Chem Soc Rev

Dynamic Article Links

Cite this: *Chem. Soc. Rev.*, 2012, **41**, 3099–3118

www.rsc.org/csr

TUTORIAL REVIEW

Diffusion in porous crystalline materials†

Rajamani Krishna*

Received 19th October 2011
DOI: 10.1039/c2cs15284c

The design and development of many separation and catalytic process technologies require a proper quantitative description of diffusion of mixtures of guest molecules within porous crystalline materials. This *tutorial review* presents a unified, phenomenological description of diffusion inside *meso*- and *micro*-porous structures. In *meso*-porous materials, with pore sizes 2 nm $< d_p <$ 50 nm, there is a central core region where the influence of interactions of the molecules with the pore wall is either small or negligible; meso-pore diffusion is governed by a combination of molecule–molecule and molecule–pore wall interactions. Within *micro*-pores, with $d_p <$ 2 nm, the guest molecules are always under the influence of the force field exerted with the wall and we have to reckon with the motion of *adsorbed* molecules, and there is no "bulk" fluid region. The characteristics and physical significance of the self-, Maxwell–Stefan, and Fick diffusivities are explained with the aid of data obtained either from experiments or molecular dynamics simulations, for a wide variety of structures with different pore sizes and topology. The influence of adsorption thermodynamics, molecular clustering, and segregation on both magnitudes and concentration dependences of the diffusivities is highlighted. In mixture diffusion, correlations in molecular hops have the effect of slowing-down the more mobile species. The need for proper modeling of correlation effects using the Maxwell–Stefan formulation is stressed with the aid of examples of membrane separations and catalytic reactors.

1. Introduction

A wide variety of ordered crystalline porous materials is used in several applications in separation and catalysis.[1,2] These include zeolites (crystalline aluminosilicates), carbon nanotubes (CNTs), metal–organic frameworks (MOFs), zeolitic imidazolate frameworks (ZIFs), covalent organic frameworks (COFs), periodic mesoporous organosilicas (PMOs), SBA-16, and MCM-41. The characteristic pore dimensions of these structures are either in the *micro*-porous ($d_p <$ 2 nm) or *meso*-porous ranges (2 nm $< d_p <$ 50 nm). Several types of channel topologies are encountered, including one-dimensional (1D) channels (*e.g.* AFI, LTL, TON, CNTs, MIL-47, MIL-53(Cr), MgMOF-74, and BTP-COF), 1D channels with side pockets (*e.g.* MOR, FER), intersecting channels (*e.g.* MFI, BEA, BOG, Zn(bdc)dabco), cavities with large windows (*e.g.* FAU, IRMOF-1, CuBTC), and cages separated by narrow windows (*e.g.* LTA, CHA, DDR, TSC, ERI, ITQ-29, ZIF-8). The structural details for zeolites are available on the website of the International Zeolite Association (IZA). Further information on the characteristic pore dimensions, pore volumes, surface areas for both zeolites and MOFs is available in the ESI† accompanying this publication. Fig. 1 presents pore landscapes for some commonly used topologies.

For reaction and separation process design and development it is necessary to have a reliable *quantitative* description of the diffusion of mixtures of guest molecules inside the porous materials. The proper description of diffusion is important for the following reasons.

(1) In many membrane separations, the permeation selectivity is significantly influenced by the relative mobilities of the adsorbed species within the pores. Indeed, in H_2-selective processes the separation relies on the fact that H_2 is more mobile than partner species such as CO_2 or CH_4.

(2) A good understanding of *correlation* effects in mixture diffusion allows us to choose the right crystalline material that has the proper mixture diffusion characteristics.

(3) In some cases of pressure swing adsorption, the separation principle is based on diffusional selectivities; this is the case for example for separation of N_2/O_2 mixtures with the LTA-4A zeolite.

Van 't Hoff Institute for Molecular Sciences, University of Amsterdam, Science Park 904, 1098 XH Amsterdam, The Netherlands. E-mail: r.krishna@uva.nl; Fax: +31 20 525 5604; Tel: +31 20 627 0990

† Electronic supplementary information (ESI) available: This material includes a document containing: (a) the pore landscapes, and structural details of a variety of meso-porous and micro-porous structures (zeolites, MOFs, ZIFs) referred to in this article, along with force fields and simulation methods. (b) Video animations to illustrate a variety of effects such as inter-cage hopping, biased-reflection in mesopore diffusion, molecular clustering, and segregation effects. See DOI: 10.1039/c2cs15284c

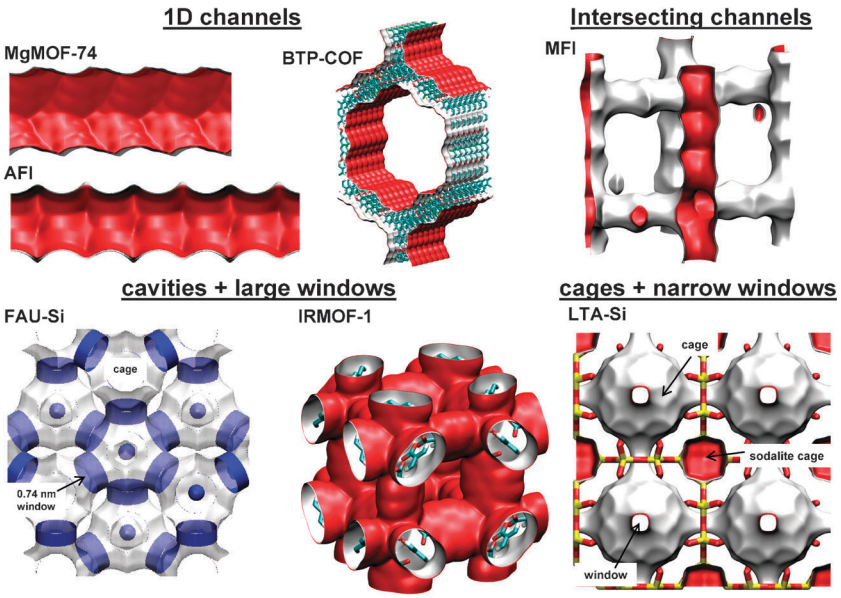

Fig. 1 Examples of the variety of channel topologies and connectivities in porous crystalline materials. Details of the specific structures are available in the ESI† accompanying this article.

(4) In catalytic processes, intra-crystalline diffusional effects affect both reaction rates and selectivities. Often, diffusional effects are undesirable because catalyst effectiveness is reduced.

The fundamental understanding of diffusion of guest molecules in porous structures is significantly aided and enhanced with the use of molecular simulation techniques: Monte Carlo (MC) simulations of adsorption isotherms in the Grand-Canonical (GC) ensemble, Molecular Dynamics (MD) simulations of diffusivities, and Transition State Theory (TST) calculations of free energy profiles and barriers. Molecular simulations are shown to be essential adjuncts to experiments. Details of simulation techniques are not provided in this article; the reader is referred to the standard ref. 3. We begin with the description of diffusion of pure component species, and subsequently move on to the description of mixture transport.

Rajamani Krishna

Rajamani Krishna received his BS (1968) and PhD (1975) degrees in Chemical Engineering from the Universities of Bombay, and Manchester, respectively. During 1970–1975, he served on the faculty of the University of Manchester, before joining the Shell group of companies in The Netherlands. During the period 1976–1984, he was involved in a wide variety of reaction and separation process developmental activities within Shell. Subsequently, he served as a Director of the Indian Institute of Petroleum, before taking up his current position of Professor at the University of Amsterdam in 1990. His research interests include adsorption and diffusion in porous materials, reactive distillation, computational fluid dynamics, membrane permeation, and pressure swing adsorption. He has published three textbooks on diffusion, has more than 390 peer-reviewed publications, and holds several patents. Currently, his h-index is 51.

2. Molecule–molecule and molecule–wall interactions

Consider the Lennard-Jones interaction potentials of some typical molecules with the pore wall; data for CH_4, Ar, and H_2 are provided in Fig. 2. The minimum in the potential energy for interaction with the wall surface occurs at a distance $= 2^{1/6}\sigma$. The depths of the potential wells characterize the energies of interaction, *i.e.* the adsorption strengths. Of the three species, CH_4 has the highest adsorption strength; the energies of interaction follow the hierarchy CH_4 > Ar > H_2. For distances greater than about 0.7 nm from the pore wall the interaction potential is virtually zero for all three species.

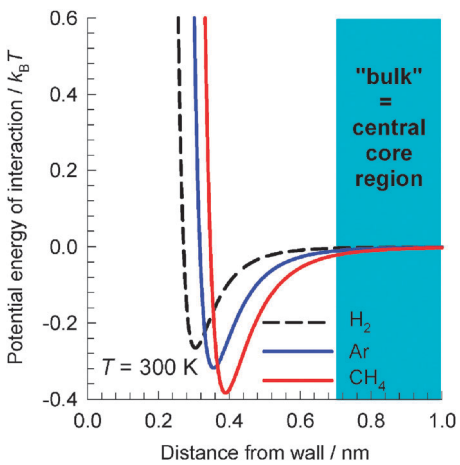

Fig. 2 The Lennard-Jones interaction potential, expressed in units of $k_B T$ for H_2, Ar, and CH_4 and a silica pore wall.

This implies that for *meso*-porous materials, with pore sizes 2 nm $< d_p <$ 50 nm, there is a central core region where the influence of interactions of the molecules with the pore wall is negligible. Conversely, for *micro*-porous materials with pore sizes smaller than about 1.4 nm, the diffusing guest molecules experience the influence of the pore walls over the *entire* pore space; *i.e.* there is no "bulk" or core region to speak of. The diffusivities in micro- and meso-pores must be expected to have fundamentally different characteristics. To highlight these differences we need to examine the diffusivities that separately characterize the molecule–molecule and molecule–pore wall interactions.

The self-diffusivity, $D_{i,\mathrm{self}}$, is determined by analyzing the mean square displacement of *individual* molecules, obtained from either molecular dynamics (MD) simulations or experimental techniques such as NMR:[4]

$$D_{i,\mathrm{self}} = \frac{1}{2}\lim_{\Delta t\to\infty}\frac{1}{n_i \Delta t}\sum_{l=1}^{n_i}\left(\boldsymbol{r}_{l,i}(t+\Delta t)-\boldsymbol{r}_{l,i}(t)\right)^2 \qquad (1)$$

The $D_{i,\mathrm{self}}$ reflects a *combination* of molecule–molecule and molecule–wall collisions.

The Maxwell–Stefan (M–S) diffusivity, $Đ_i$, that characterizes molecule–wall interactions, is obtained by monitoring the mean square displacement of an *ensemble* of molecules[4]

$$Đ_i = \frac{1}{2}\lim_{\Delta t\to\infty}\frac{1}{n_i \Delta t}\left(\sum_{l=1}^{n_i}\left(\boldsymbol{r}_{l,i}(t+\Delta t)-\boldsymbol{r}_{l,i}(t)\right)\right)^2 \qquad (2)$$

If we define the self-exchange coefficient $Đ_{ii}$ as a diffusivity characteristic of molecule–molecule interactions, we get the interpolation formula for self-diffusivity

$$1/D_{i,\mathrm{self}} = 1/Đ_i + 1/Đ_{ii} \qquad (3)$$

Eqn (3), formally valid for *both* micro- and meso-porous materials, will be derived in a later section starting with the M–S equations for binary mixture diffusion for identical species, tagged and un-tagged. A combination of eqn (1)–(3) yields the self-exchange coefficient $Đ_{ii}$. At any loading $D_{i,\mathrm{self}} \leq Đ_i$; this is because individual jumps of molecules are *correlated* due to re-visitation of sites that have been recently abandoned. The $Đ_i$, reflecting *collective* motion of molecules (*cf.* eqn (2)), is free from such correlation effects; it is for this reason that the $Đ_i$ is amenable to simpler interpretation, and modeling, than the $D_{i,\mathrm{self}}$.

For practical applications, it is more common to use the Fick diffusivity D_i that relates the flux N_i of species i to the gradient of the pore concentration

$$N_i = -\phi D_i \nabla c_i \qquad (4)$$

The fluxes N_i used in eqn (4) are defined using a reference velocity frame with respect to the host structure and are expressed in terms of the cross-sectional area of the crystalline material; it is for this reason that the fractional pore volume of crystalline material, ϕ, appears as a multiplicative factor. The pore concentrations c_i are expressed as the number of moles per m^3 of *accessible* pore volume. Many microporous structures contain pockets or cages that are not accessible in experiments. In molecular simulations, it is important to block such regions in order to obtain a fair representation of experimental reality. For example, the sodalite cages in LTA-Si, ITQ-29, FAU, and TSC need to be blocked as these are inaccessible to guest molecules; *cf.* Fig. 1. DDR zeolite contains pockets that need blocking. The accessible pore volume can be determined with the aid of molecular simulations using the helium probe insertion technique.[5] Factors for converting loadings expressed in molecules per unit cell or moles per kg of framework to the pore concentrations, c_i, for all structures discussed in this review are provided in the ESI.† The Fick diffusivity, also referred to as the "transport" diffusivity, is related to the M–S, or "corrected", diffusivity $Đ_i$ by[1]

$$D_i = Đ_i \Gamma_i \qquad (5)$$

where the thermodynamic factor Γ_i, determinable from adsorption equilibrium data, is defined by

$$\frac{c_i}{RT}\nabla\mu_i \equiv \Gamma_i \nabla c_i; \quad \Gamma_i \equiv \frac{\partial \ln f_i}{\partial \ln c_j} = \frac{c_i}{f_i}\frac{\partial f_i}{\partial c_i} \qquad (6)$$

The thermodynamic factor can be determined directly from molecular simulations, or from differentiation of the adsorption isotherm. The Fick diffusivity, determined from say uptake or chromatographic experiments,[1] is *directly* influenced by adsorption thermodynamics and is therefore much more difficult to interpret from a fundamental viewpoint. The approach we shall adopt here is to seek a physical understanding of the variety of factors that *separately* influence $D_{i,\mathrm{self}}$, $Đ_i$, $Đ_{ii}$, and Γ_i.

The degree of correlations

The relative importance of molecule–molecule and molecule–wall interactions is extremely important in the description of mixture diffusion. We can define the *degree of correlations* as the ratio $Đ_i/Đ_{ii}$; the larger the value of this ratio, the stronger is the relative influence of molecule–molecule interactions. A higher value of $Đ_i/Đ_{ii}$ results in stronger *coupling* effects in mixture diffusion, to be elaborated later. The degree of correlations also depends on the pore size, connectivity and topology. Fig. 3 presents a comparison of $Đ_i/Đ_{ii}$ for H_2 and CH_4 diffusion in a variety of host materials. Broadly speaking, the highest degree of correlations is for 1D channel structures, such as MgMOF-74 and BTP-COF, because of the difficulty of *by-passing* of molecules. The smallest degree of correlations is realized in structures such as LTA-Si, CHA, SAPO-34, DDR, ITQ-29, and ZIF-8 that have cages separated by windows that are in the 0.32 nm to 0.41 nm size range. In such structures, the inter-cage hops across the window occur one-molecule-at-a-time and correlations are practically negligible at pore concentrations $c_i <$ 10 kmol m^{-3} and we have the approximations $Đ_i/Đ_{ii} \approx 0$ and $D_{i,\mathrm{self}} \approx Đ_i$.[4] For concentrations $c_t >$ 10 kmol m^{-3}, intra-cage motion becomes limiting leading to sizable correlation effects even in such cage structures. It is remarkable to note that mesoporous BTP-COF has the highest degree of correlations. Molecule–molecule interactions are relatively strong in *meso*porous materials, and this is not an intuitively obvious result.

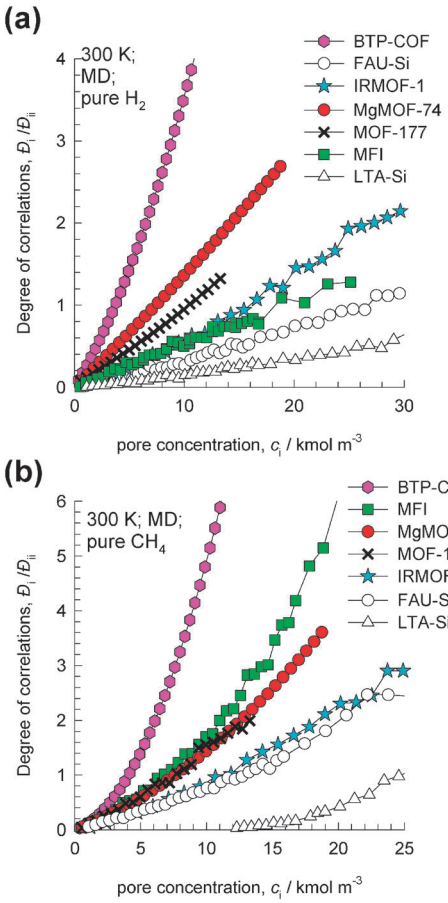

Fig. 3 The degree of correlations, $Đ_i/Đ_{ii}$, for diffusion of (a) H_2, and (b) CH_4 in a variety of porous host materials.[8]

3. Knudsen and Bosanquet prescriptions for mesoporous materials

For diffusion in meso-porous materials, two further assumptions are commonly made in using eqn (3). The first assumption is that the self-exchange coefficient $Đ_{ii}$ can be identified with the self-diffusivity in the *fluid* phase, $Đ_{ii,fl}$. Secondly, the M–S diffusivity, $Đ_i$, is commonly calculated for mesopores from the Knudsen formula[1]

$$D_{i,\mathrm{Kn}} = \frac{d_\mathrm{p}}{3}\sqrt{\frac{8RT}{\pi M_i}} \qquad (7)$$

Setting $Đ_{ii} = Đ_{ii,fl}$ and $Đ_{ii} = D_{i,Kn}$ in eqn (3) yields the widely used Bosanquet equation. It is instructive to test the Bosanquet formula by considering diffusion of H_2 and CH_4 within the 3.4 nm channels of the covalent organic framework BTP-COF. The MD simulated values of $Đ_{ii}$, $D_{i,self}$, and $Đ_i$ are presented in Fig. 4 for a range of pore concentrations. Fig. 4a shows that the values of $Đ_{ii}$ for both H_2 and CH_4 are in excellent agreement with *fluid* phase, $Đ_{ii,fl}$, obtained also from MD. For pore concentrations $c_i < 10$ kmol m^{-3} both sets of values are in agreement with the calculations using the correlation of Fuller, Schettler and Giddings (FSG), developed for *ideal gas* mixtures. The results in Fig. 4a are valid for a wide range of guest–mesoporous host combinations, and are of great practical utility because they allow molecule–molecule interactions to be quantified from *fluid*-phase diffusivity data and correlations.

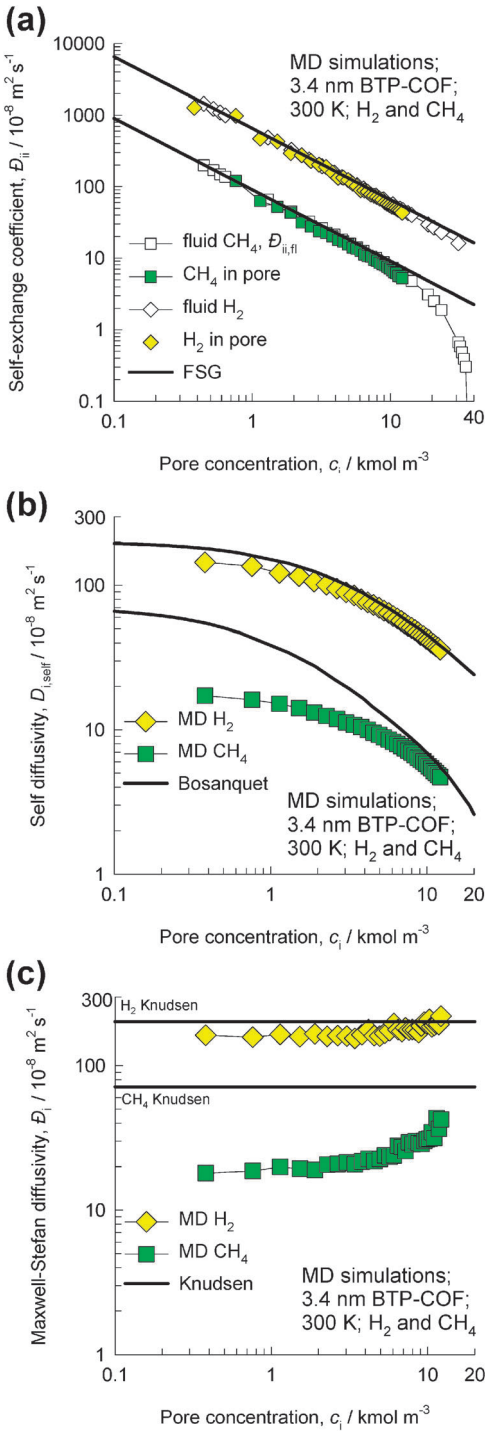

Fig. 4 MD simulations of (a) self-exchange coefficients, $Đ_{ii}$, (b) self-diffusivities, $D_{i,self}$, and (c) M–S diffusivities, $Đ_i$, of H_2 and CH_4 in BTP-COF, a covalent organic framework with 3.4 nm pore size, as a function of the pore concentration c_i. The MD simulations (symbols) are compared with the estimations using the Bosanquet and Knudsen formulae. In (a) the correlation of Fuller, Schettler and Giddings (FSG),[50] developed for *binary* gas mixtures, is employed by taking both species to be identical to each other.

For H_2, which has poor adsorption strength, the MD simulated values of $D_{i,self}$ are in reasonably good agreement with the calculations using eqn (3) for the entire range of pore

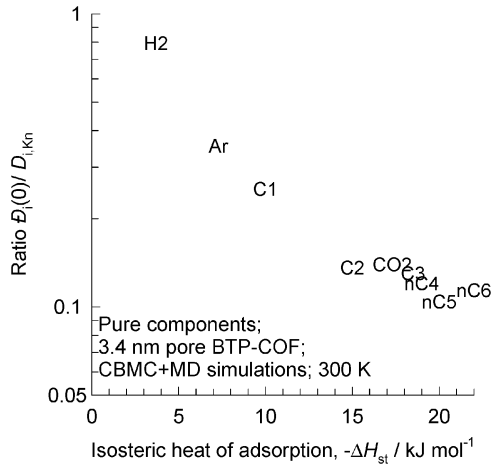

Fig. 5 Ratio of the MD data on the zero-loading M–S diffusivity to the calculated Knudsen diffusivity, $Đ_i(0)/D_{i,Kn}$, for hydrogen, argon, carbon dioxide (CO_2), methane (C1), ethane (C2), propane (C3), *n*-butane (*n*C4), *n*-pentane (*n*C5), and *n*-hexane (*n*C6) plotted as a function of the isosteric heat of adsorption $-\Delta H_{st}$ of the corresponding species. The $Đ_i(0)$ is obtained from MD data extrapolation.

concentrations; see Fig. 4b. For CH_4, the Bosanquet formula severely over-estimates the self-diffusivities at low pore concentrations where molecule–wall interactions are dominant. To elucidate this further, we would need to examine the validity of the Knudsen prescription by comparing the calculations of $D_{i,Kn}$ with MD simulated $Đ_i$. From Fig. 4b we note that the Knudsen formula is a reasonably good approximation for H_2 but severely over-estimates the CH_4 diffusivity by a factor of about five. The Knudsen prescription demands that the reflections are purely *diffuse* in nature, *i.e.* the angle of reflection bears no relation to the angle of incidence at which the molecule strikes the pore wall. Adsorption at the pore wall introduces a *bias* that makes a molecule hop to a neighboring site on the surface rather than return to the bulk; this bias increases with increasing adsorption strength.[6] The bias is best appreciated by viewing video animations of MD simulations, provided as ESI†, showing the hopping of hydrogen, argon, carbon dioxide, and methane within the 1D channel of BTP-COF.

The isosteric heat of adsorption, $-\Delta H_{st}$, may be taken as a measure of the adsorption strength, or binding energies, for each species. The extent of deviations from the Knudsen prescription appears to correlate well with the isosteric heat of adsorption; see Fig. 5. The stronger the binding energy the stronger the deviations from the Knudsen formula.

4. Characteristics of diffusivities in microporous materials

The Knudsen and Bosanquet prescriptions are of little relevance to microporous materials; the molecule–molecule and molecule–wall interactions within micropores exhibit much richer and more complex behaviors. For any guest molecule, the magnitudes of the diffusivities, and their dependences on c_i are dictated by a variety of factors including pore size, topology, and connectivity, and adsorption isotherm characteristics.[1,4,7]

Molecule–molecule interactions in micropores

Within micro-pores, molecule–molecule interactions are additionally influenced by interactions with the walls. Fig. 6a and b illustrates this for H_2 and CH_4 diffusion in six typical microporous structures: IRMOF-1, MOF-177, MgMOF-74, FAU-Si, LTA-Si, and MFI. The values of $Đ_{ii}$ are consistently

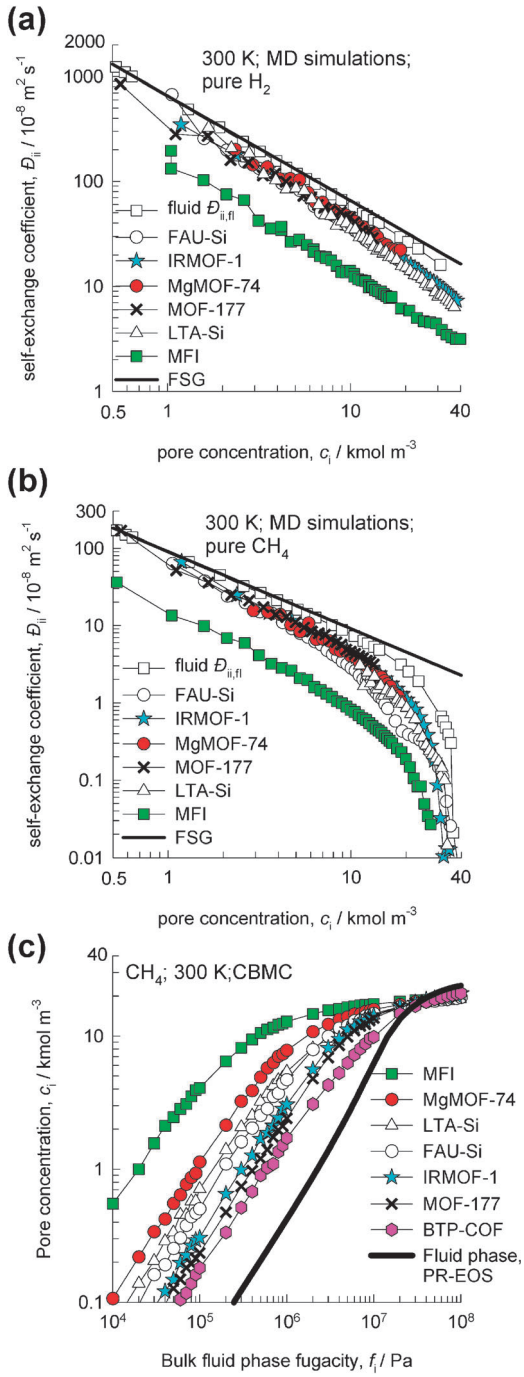

Fig. 6 (a, b) MD simulations[4,8,51] of self-exchange coefficients, $Đ_{ii}$, for diffusion of (a) H_2, and (b) CH_4 in IRMOF-1, MgMOF-74, FAU-Si, LTA-Si, and MFI, as a function of the pore concentration c_i. The continuous solid lines represent the correlation of Fuller, Schettler and Giddings (FSG).[50] (c) CBMC simulations of adsorption isotherms for pure CH_4 in zeolites and MOFs.

lower than the fluid phase $Đ_{ii,\mathrm{fl}}$. The extent of lowering correlates with the *degree* of confinement.[7] The molecules are most strongly confined within the 0.55 nm channels of the MFI zeolite, and the values of $Đ_{ii}$ are lower than $Đ_{ii,\mathrm{fl}}$ by a factor of about 10. A further point to note is that the values of self-exchange $Đ_{ii}$ for CH_4 appear to converge to the value of $Đ_{ii,\mathrm{fl}}$ as the pore concentrations c_i approach the value of the molar density of the *liquid* phase, which is approximately 35 kmol m^{-3}. The molar liquid density provides a good estimate of the saturation capacity, $c_{i,\mathrm{sat}}$, of a guest molecule within the pores. To confirm this Fig. 6c presents Configurational-Bias Monte Carlo (CBMC) simulations of the pure component isotherms of CH_4. The isotherms for a variety of structures, including the mesoporous BTP-COF, converge to a saturation capacity value of 35 kmol m^{-3}. Also plotted in Fig. 6c is the calculation of the *fluid phase* molar density using the Peng–Robinson equation of state for CH_4 at 300 K, which confirms that the molar liquid density of 35 kmol m^{-3} is a good approximation for the saturation capacity of CH_4 in *all* porous materials; this is a general and useful conclusion.[7]

Influence of binding energy on adsorption

Broadly speaking, the hierarchy of diffusivity values is dictated by two factors: (1) the characteristic pore dimensions, and (2) the binding energy of the guest species. For illustration purposes, Fig. 7a presents MD simulated $D_{i,\mathrm{self}}$ data for pure CO_2 in a few chosen microporous structures. Fig. 7b presents the corresponding data on the isosteric heats of adsorption of CO_2 within a variety of structures; these data give a good reflection of the hierarchy of the binding energies. Consider the three structures FAU-Si (*i.e.* all-silica), NaY (54 Na^+ per unit cell), and NaX (86 Na^+ per unit cell) that have the same pore topology with pore dimension (window aperture) of 7.4 Å, but with increasing number of cations. Increasing the number of cations increases the binding energy of CO_2, due to increased electrostatic interactions. From Fig. 7b we note that the heats of adsorption follow the hierarchy NaX > NaY > FAU-Si, and this explains why the $D_{i,\mathrm{self}}$ values for CO_2 have the inverse hierarchy FAU-Si > NaY > NaX. A higher sticking tendency implies a lower mobility.[4] Fig. 7b also shows that the heat of adsorption of CO_2 in MgMOF-74 is significantly higher than for ZnMOF-74; the stronger binding energy with Mg atoms accounts for the significantly lower diffusivity of CO_2 in MgMOF-74 when compared to ZnMOF-74, despite the fact that the channel dimensions of these two MOFs are the same, both being 11 Å. The inescapable conclusion that is to be drawn from the foregoing discussions is that, generally speaking, adsorption and diffusion do not go hand in hand. A stronger adsorption strength implies a lower diffusivity, and this has ramifications for membrane separations.[8]

Diffusivities in cage-type structures with narrow windows

Cage-type structures such as LTA, CHA, DDR, TSC, ERI, ZIF-7, and ZIF-8 have potential applications in the separation of mixtures such as CO_2/CH_4, CO_2/H_2, H_2/CH_4, ethene/ethane, and propane/propene.[2,9,10] The separation principle is based not only on the differences in the adsorption characteristics, but also on the differences in the diffusivities of the

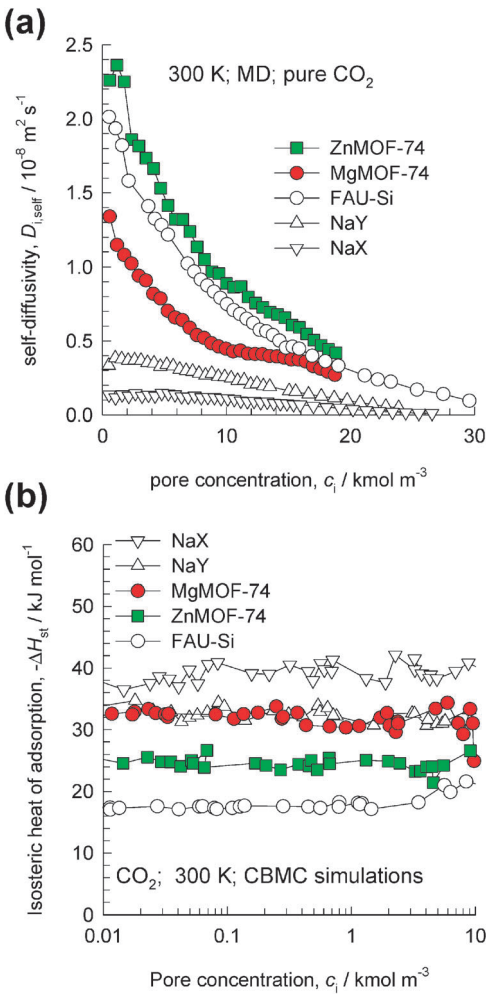

Fig. 7 (a) Self-diffusivity $D_{i,\mathrm{self}}$, from MD simulations for pure CO_2 in a variety of microporous materials: FAU-Si, NaY (144 Si; 48 Al; 48 Na^+; Si/Al = 3), NaX (106 Si; 86 Al; 86 Na^+; Si/Al = 1.23), MgMOF-74, and ZnMOF-74, as a function of the pore concentration c_i.[2] (b) CBMC simulations of the isosteric heats of adsorption of CO_2.

guest molecules across the windows that are typically in the 3.2 Å to 4.1 Å size range. For example, the window dimensions for DDR are $d_{\min}$ = 3.65 Å and $d_{\max}$ = 4.37 Å; see Fig. 8a. The diffusivity of molecules is primarily dictated by the *degree of confinement* the guest molecule experiences at the window regions. The window offers high free energy barriers for inter-cage hopping. The significance of the window dimension is best illustrated by comparing the $D_{i,\mathrm{self}}$ values for CH_4 in different structures at a low pore concentration value of c_i = 1 kmol m^{-3}; see Fig. 8b. Increasing the window aperture from 3.65 for DDR to 4.1 Å for LTA-Si (all-silica) results in an increase in $D_{i,\mathrm{self}}$ by about two orders of magnitude. These data trends are in qualitative agreement with the PFG NMR data presented by Hedin *et al.*[11] From a practical point of view, the data trends help in the choice of the zeolite for kinetic separations by appropriate tuning of the window dimensions. Care must however be exercised in extrapolating the trends to ZIF-7 or ZIF-8 that have windows of 3.26 Å.[9,10] In these cases there is evidence that the window dynamics are significantly different to that of 8-ring zeolites, and subject to guest-specific "gate opening".[12]

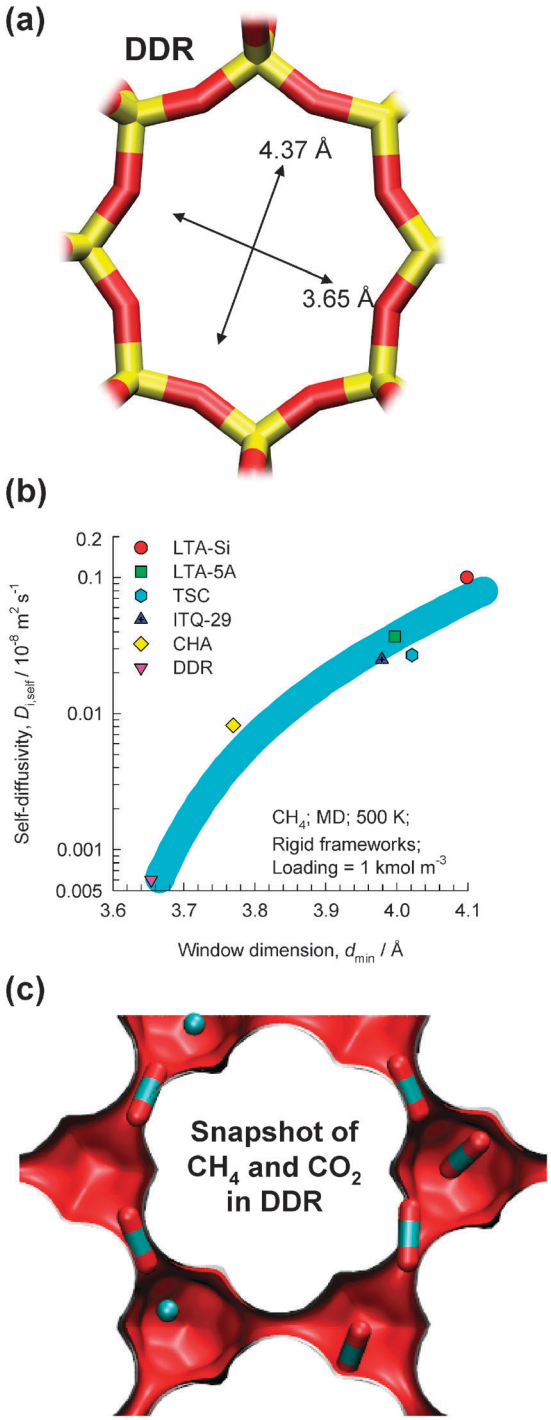

Fig. 8 (a) Window dimensions for DDR. Two dimensions of the 8-ring window are indicated: the shortest ("straight") distance, d_{min}, and the longest ("diagonal") distance, d_{max}. (b) Values of $D_{i,self}$, determined at a concentration c_i = 1 kmol m^{-3}, plotted as a function of the window dimension d_{min} for various cage-type zeolites. (c) Snapshot showing the location of CH_4 and CO_2 molecules in DDR.

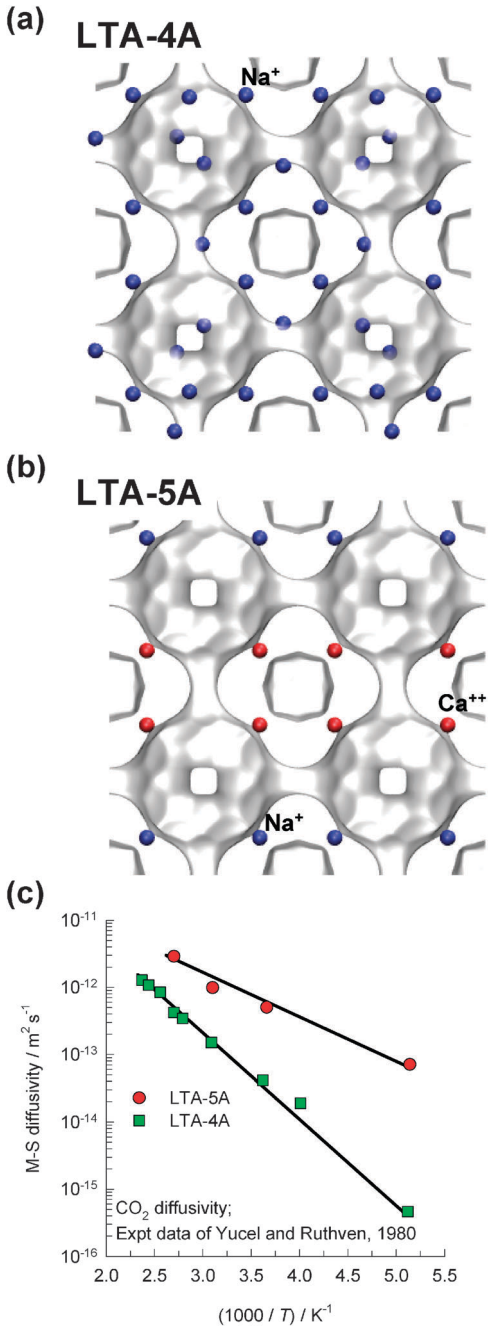

Fig. 9 (a, b) Snapshots showing the location of cations in (a) LTA-4A, and (b) LTA-5A. (c) Arrhenius plots of the experimental data of Yucel and Ruthven[52] for M–S diffusivity of CO_2 in LTA-4A, and LTA-5A.

In LTA-4A, some of the Na^+ cations locate at the 8-membered ring window regions[13] (*cf.* Fig. 9a) and hinder inter-cage hopping. The Na^+ and Ca^{++} cations in LTA-5A, on the other hand, do not occupy the window regions (*cf.* Fig. 9b). Partial blocking of the windows explains why the diffusivity of CO_2 in LTA-4A is about 1–3 orders of magnitude lower than that within LTA-5A; see data in Fig. 9c.

"Linear" molecules such as CO_2, N_2, and O_2 hop lengthwise across the windows; this is illustrated by the snapshot Fig. 8c showing the location of CH_4 and CO_2 molecules in DDR. A qualitative appreciation of the length-wise hops of CO_2 across the windows is obtained from video animations for inter-cage hopping across the windows of LTA-Si, and DDR that are available as ESI.† The relevant dimension of CO_2 that determines the diffusivity is the *cross-sectional diameter*; the commonly used "kinetic" diameter is irrelevant. Due to the

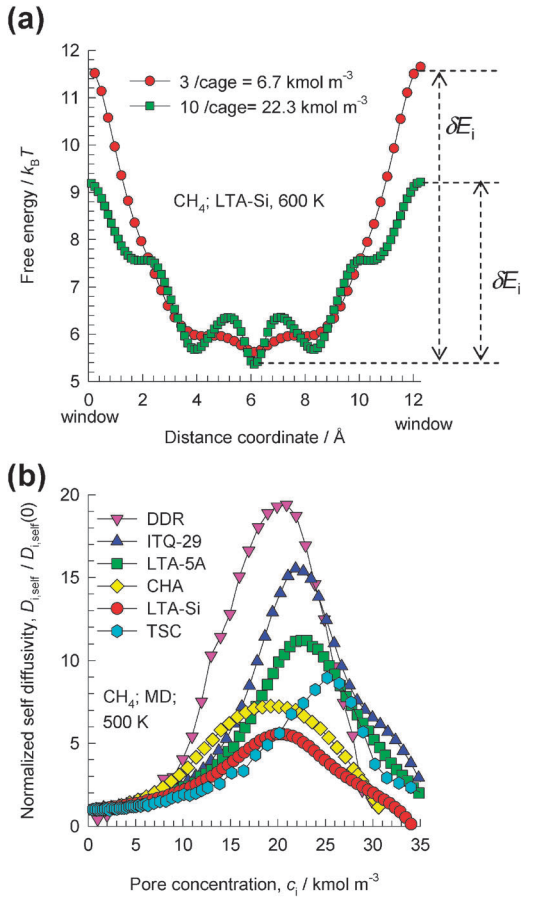

Fig. 10 (a) Free energy profiles for CH_4 in LTA (all-silica) at 600 K, determined by molecular simulations for loadings of 3 and 10 molecules per cage.[22] (b) MD simulations of the self-diffusivities, $D_{i,self}$, normalized with respect to the zero-concentration value $D_{i,self}(0)$, of CH_4 in CHA, LTA-5A, ITQ-29, TSC, and LTA-Si zeolites at 500 K.

lengthwise hops, the diffusivities of CO_2 are higher than those for CH_4 by about two orders of magnitude for LTA-Si, CHA, DDR, TSC, and ERI. This explains the efficacy of such zeolites for use in CO_2-selective membrane separations.

The concentration dependences of the diffusivities in cage-type structures are somewhat complex, and require quantification of the free energy barriers for inter-cage hopping. The free energy barrier for inter-cage hopping, δE_i, may be defined as the difference between the values of free energy at the window and within the cages. Typical free energy profiles for CH_4 in LTA-Si, for loadings of 3 and 10 molecules per cage, are shown in Fig. 10a.[14] We note that with increased loading, the free energy of molecules within a cage increases due to molecule–molecule interactions. As a result, δE_i decreases with increased loading; *cf*. Fig. 10a. A consequence of the reduction of δE_i is a diffusivity increase, as witnessed by data on normalized diffusivities presented in Fig. 10b. The increase of $D_{i,self}$ with c_i is not monotonic because the cage capacity is limited and there are fewer intra-cage vacant sites to occupy. As the saturation loading is approached, progressively fewer vacant sites become available. The net result is that $D_{i,self}$ displays a maximum and decreases thereafter as $c_i \to c_{i,sat} \approx 35$ kmol m^{-3}.

Diffusivities in "large" channels and in "open" structures

For diffusion in microporous structures with characteristic channel dimensions larger than say 7.3 Å, there are no discernible regions that afford high energy barriers to molecular jumps. The situation is much simpler than discussed in the foregoing section; a molecule can jump from one adsorption site to an adjacent one, provided it is not already occupied. The simplest model to describe the concentration dependence is

$$Đ_i = Đ_i(0)(1 - \theta_i) \tag{8}$$

where $Đ_i(0)$ is the diffusivity in the limiting case of vanishingly small *fractional occupancy*, defined by

$$\theta_i = c_i/c_{i,sat} \tag{9}$$

The key to the quantification of the concentration dependence of $Đ_i$ is to determine how the vacancy $(1 - \theta_i)$ changes with increased pore concentration. This information is contained in the *inverse thermodynamic factor* $1/\Gamma_i$. If the adsorbed phase concentration follows a single-site Langmuir isotherm

$$c_i = c_{i,sat}\frac{b_i f_i}{1 + b_i f_i} \tag{10}$$

then we obtain from eqn (6)

$$1/\Gamma_i = (1 - c_i/c_{i,sat}) = (1 - \theta_i) \tag{11}$$

Eqn (11) shows that inverse thermodynamic factor, $1/\Gamma_i$, equals the fractional *vacancy* $(1 - \theta_i)$. In the general case where the component adsorption exhibits inflection behavior, due perhaps to second-order phase transitions, $1/\Gamma_i$ provides a good indicator of how the availability of adsorption sites changes with increased bulk fluid phase fugacity. We can generalize eqn (8) to cater for more complex adsorption isotherm characteristics by writing

$$Đ_i = Đ_i(0)\frac{1}{\Gamma_i} \tag{12}$$

The data for diffusivities of CH_4 in AFI and FAU-Si, both with characteristic dimension of 7.4 Å, confirm the validity of eqn (12); see Fig. 11. Particularly noteworthy is that the mild inflections in $1/\Gamma_i$ get reflected in the corresponding inflections in the $Đ_i - c_i$ dependence.

Strong isotherm inflections

Preferential location of molecules within the structural framework can cause strong isotherm inflections. For example, branched alkanes, benzene, alkyl benzenes, and cyclohexane prefer to locate at the channel intersections of MFI zeolite due to extra "leg-room" and other configurational considerations.[15] A snapshot of the location of iso-butane (iC4) is shown in Fig. 12a as illustration. There are only 4 intersection sites available per unit cell of MFI. This implies that to obtain loadings higher than $\Theta_i = 4$ molecules per unit cell, an extra "push" will be required to locate the molecules elsewhere within the channels; this leads to isotherm inflection; see CBMC simulated isotherms of iC4, 2-methylpentane (2MP), and 2,2-dimethylbutane (22DMB) in Fig. 12b. Due to strong inflections, the $1/\Gamma_i$ of branched alkanes in MFI shows a cusp-like inflection at a loading of $\Theta_i = 4$, when all the preferred

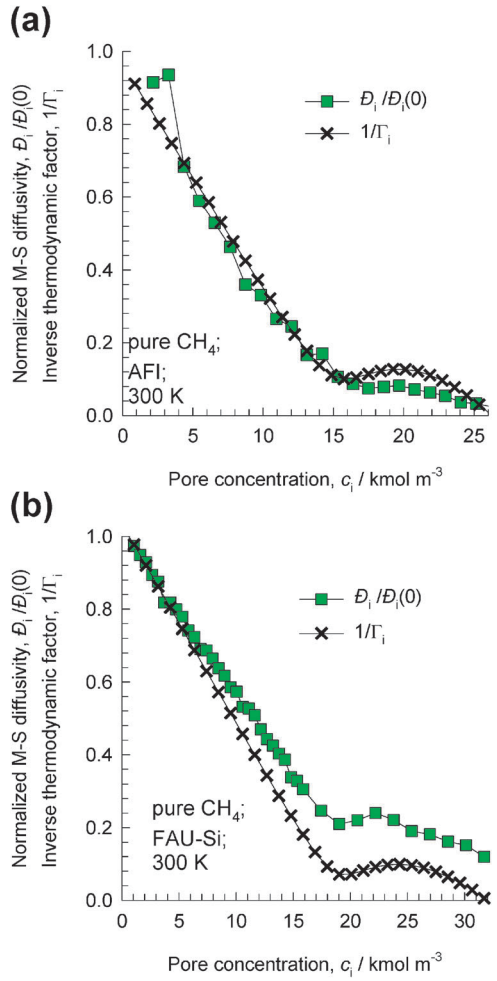

Fig. 11 Comparison of the concentration dependences of the normalized M–S diffusivity, $Đ_i$, and inverse thermodynamic factor, $1/\Gamma_i$, for CH_4 in (a) FAU-Si, and (b) AFI.[4] The $1/\Gamma_i$ is determined from analytic differentiation of the CBMC simulated isotherms.

adsorption sites are occupied; see Fig. 12c. In the range $0 < \Theta_i < 4$, $1/\Gamma_i$ decreases nearly linearly with Θ_i signifying the fact that the vacancy *decreases* almost linearly with loading. For $\Theta_i > 4$, $1/\Gamma_i$ increases with Θ_i because additional sites *within* the MFI channels are created to accommodate more than 4 molecules per unit cell, *i.e.* the number of available sites *increases* within this loading range. These additional sites are within the channels, requiring the additional "push" that caused the inflection. The $Đ_i$ data in Fig. 12d, determined from uptake of iC4 within MFI crystals using infra-red microscopy (IRM), show a sharp cusp-like minimum at $\Theta_i = 4$ in agreement with eqn (12).[16] This cusp-like $Đ_i - \Theta_i$ relation was anticipated by Kinetic Monte Carlo (KMC) simulations. The experimental data for $Đ_i$ of benzene in MFI show similar behavior and are caused by the same reasons as illustrated for iC4.[17]

Non-monotonic variation of diffusivity with the chain length

For diffusion of a homologous series of chain molecules there could be either a match, or mismatch, between the characteristic periodicity of the host structure and the characteristic length of the guest molecules. From Fig. 1 we note a periodicity in the potential energy landscape, caused due to a variety of factors. For 1D channel structures AFI, LTL, TON, and MTW there is a characteristic segment length. For MFI, ISV, and BOG the periodicity is introduced by the distances between channel intersections. For cage-type zeolites LTA, DDR, CHA, TSC, ERI, and ZIF-8 the periodicity is introduced by the window-to-window distance. The net result could be a non-monotonic variation of the diffusivity with the chain length. This non-monotonicity has been given a variety of names in the literature: resonant diffusion,[18–20] window effect,[21] and commensurate–incommensurate diffusion.[22] As illustration, the QENS data of Jobic *et al.*[23] for diffusivity in LTA-5A with increasing n-alkane chain length display a minimum value for nC8; see Fig. 13a. Snapshots showing the conformations of nC8 and nC13 molecules within the cages of LTA-5A provide a rationale for the non-monotonicity (Fig. 13b and c). nC8 can nestle comfortably within a single cage, whereas nC13 is too long, *i.e.* incommensurate with the window-to-window distance, and straddles two adjacent cages. An incommensurate scenario leads to a higher diffusivity because the molecule does not feel "too comfortable" and has a tendency to hop with increased frequency.

The length of an nC6 alkane molecule is commensurate with the distance between intersections of MFI zeolite (*cf.* snapshot in Fig. 14a), and this causes a non-monotonic dependence of diffusivities on the chain length (*cf.* Fig. 14b). This explains why the experimental data obtained from membrane permeation[24] show a minimum in the diffusivity for nC6. A further consequence is that n-alkanes with 6 or more C atoms show strong isotherm inflections, leading to a corresponding inflection in the loading dependence of the diffusivities.[25]

Molecular clustering

A molecular cluster can be regarded as a *k*-mer; for example a dimer. The characteristic signature of cluster formation is that the adsorption isotherm exhibits a steep increase in the loading, with the inverse thermodynamic factor exceeding unity, *i.e.* $1/\Gamma_i > 1$, for a range of pore concentrations. A *k*-mer occupies the same vacant adsorbed site as a normal, unclustered, molecule, and the fractional vacancy can exceed unity. There are two major causes of molecular clustering, discussed below in turn.

Firstly, when the temperature T is lower than the critical temperature, T_c, the adsorbed phase is in a meta-stable thermodynamic state, and this leads to the possibility of cluster formation. For example, the critical temperature of CO_2 is 301 K, and there is a significant amount of cluster formation for adsorption at temperatures lower than 300 K. Due to cluster formation the isotherms become increasingly steeper as the temperature is lowered; this is witnessed in CBMC simulations for CO_2 isotherms in IRMOF-1 for a variety of temperatures; see Fig. 15a. The observed data are in good quantitative agreement with the experiments of Walton *et al.*[26] The steepness of the isotherms can only be properly captured by using the dual-site Langmuir–Freundlich isotherm

$$q_i = q_{i,A,\mathrm{sat}} \frac{b_{i,A} f_i^{\nu_{i,A}}}{1 + b_{i,A} f_i^{\nu_{i,A}}} + q_{i,B,\mathrm{sat}} \frac{b_{i,B} f_i^{\nu_{i,B}}}{1 + b_{i,B} f_i^{\nu_{i,B}}} \qquad (13)$$

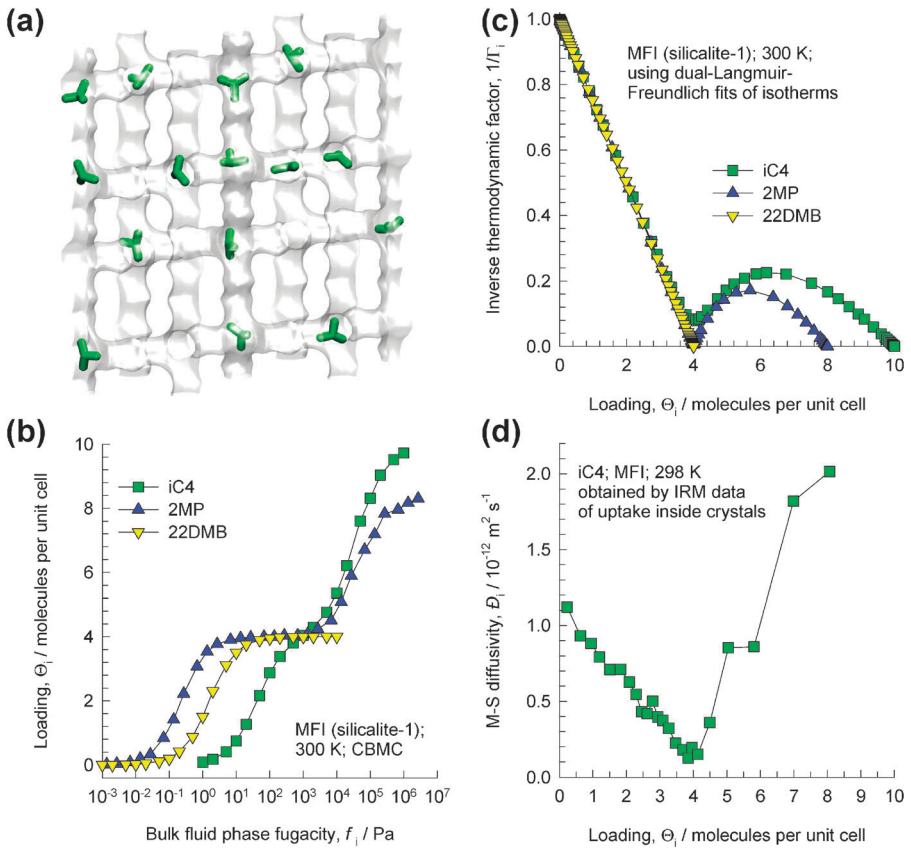

Fig. 12 (a) Snapshot showing the location of iC4 in MFI at a loading of 4 molecules per unit cell. (b) CBMC simulations of the pure component isotherms for iC4, 2MP, and 22DMB in MFI at 300 K. (c) The inverse thermodynamic factor, $1/\Gamma_i$, plotted as a function of the loading, Θ_i, for adsorption of iC4, 2MP, and 22DMB in MFI at 300 K. (d) M–S diffusivity, $Đ_i$, and $Đ_i(0)/\Gamma_i$ for iso-butane diffusion in MFI zeolite.[16]

with at least one of the exponents exceeding unity; the fits are shown by the continuous solid lines. As T falls progressively below T_c, $1/\Gamma_i$ exceeds unity to increasingly greater extents indicating increased levels of clustering; see Fig. 15b. Neutron diffraction experiments confirm the clustering of CO_2 molecules within carbon nanopores.[27] The neutron diffraction experiments of Getzschmann *et al.*[28] for adsorption of CH_4 in CuBTC provide conclusive evidence that the steepness of the isotherms is related to cluster formation, and that clustering becomes more predominant as the temperature is lowered below T_c. Importantly, the Getzschmann experimental data on the isotherms are essentially captured by molecular simulations, providing support to the arguments presented here. A further consequence of cluster formation is that the isosteric heats of adsorption are significantly higher at lower T; see Fig. 15c.

The second reason for clustering within pores is due to hydrogen bonding. Hydrogen bonding manifests for guest molecules such as water and alcohols, and in regions where cluster formation occurs we have $1/\Gamma_i > 1$; Fig. 15d illustrates this for methanol and ethanol adsorption within the cages of ZIF-8. Radial distribution functions showing the intermolecular distances provide conclusive proof of the existence of molecular clusters.[29] A visual appreciation of methanol clustering in ZIF-8 is provided by the snapshots in Fig. 15e. It is also apparent from this snapshot that there is also a tendency for molecules to congregate, leading to unequal cage occupancies. The influence of clustering on mobilities can be qualitatively appreciated by viewing the video animations, available as ESI†, of diffusion of water, methanol, and ethanol in DDR zeolite.

There are a number of quantitative consequences of molecular clustering on diffusion characteristics. In general, we should expect molecular clusters to have a lower mobility than that of the unclustered state. Coupled with the fact that with increased temperature, the degree of clustering is lower (*cf.* Fig. 15b), we conclude that the T-dependence of diffusivities may exhibit a non-Arrhenius character.[30,31] Clustering also influences the concentration dependence of the diffusivities. The concentration dependences of M–S diffusivity $Đ_i$ may indicate a maximum, as a direct consequence of the maximum in the $1/\Gamma_i$ *vs.* c_i behaviors. In cases where clustering effects are strong, the corresponding $D_{i,\mathrm{self}}$ could also display a maximum in its dependence on pore concentration. This leads to the Type IV behavior in the Kärger and Pfeifer classification of concentration dependences.[32] Fig. 16 presents three examples of experimental observation of Type IV characteristics. The maximum in the nC6 diffusivity in NaCaX is due to the fact that $T = 293$ K is significantly lower than $T_c = 507.4$ K for nC6. The critical temperature of CH_4 is 191 K, and at $T = 200$ K, close to T_c, there is a tendency for cluster formation to be induced. This is the most likely cause of the maximum in CH_4 diffusivity in the QENS data for NaY; see Fig. 16b.[33] The maximum in the methanol diffusivity in NaX (*cf.* Fig. 16c) is traceable to hydrogen bonding effects, causing $1/\Gamma_i > 1$.[33,34]

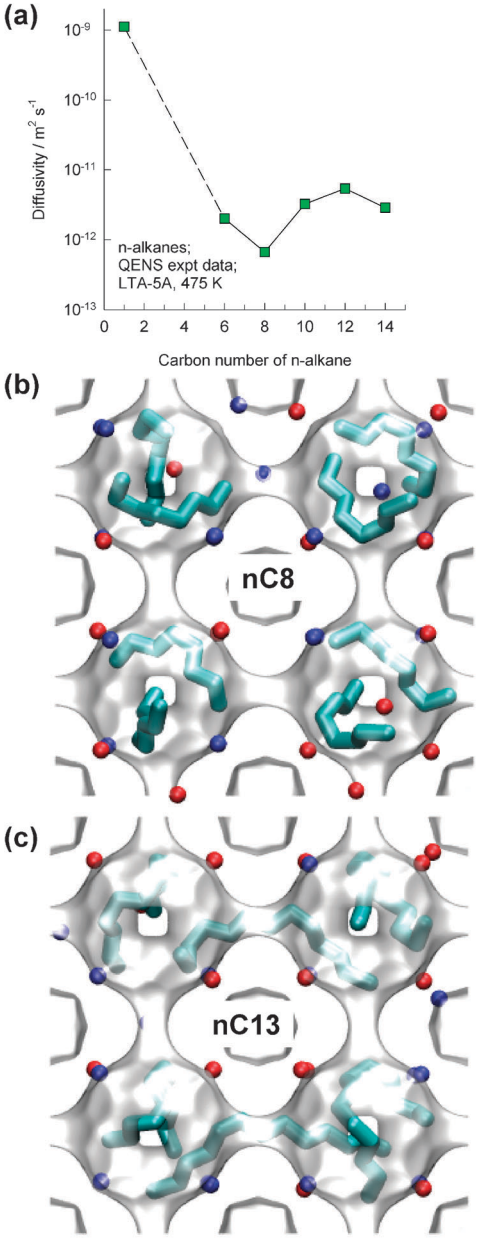

Fig. 13 (a) QENS data of Jobic *et al.*[23] for diffusivity of n-alkanes in LTA-5A. (b, c) Snapshots showing the conformations of (b) nC8 and (c) nC13 alkanes within the cages of LTA-5A.

In concentration regions where $1/\Gamma_i > 1$, eqn (5) would yield the hierarchy $D_i < Đ_i \leq D_{i,\text{self}}$. Experimental confirmation of this unusual hierarchy is found for diffusion of methanol and ethanol in ZIF-8; see Fig. 17. The unusual hierarchy of diffusivities is confined to concentrations regions for which $1/\Gamma_i > 1$ in Fig. 15d. Without invoking the concept of molecular clustering it is not possible to explain the experimental data shown in Fig. 17. The experimental investigations of Salles *et al.*[35,36] for CO_2 diffusion in MIL-47 and MIL-53(Cr)-lp provides further confirmation of the unusual trends resulting from clustering at $T = 230$ K $< T_c$.

Surface resistance

The surfaces of crystalline materials may possess diffusion characteristics that are distinct from the bulk of the crystal.

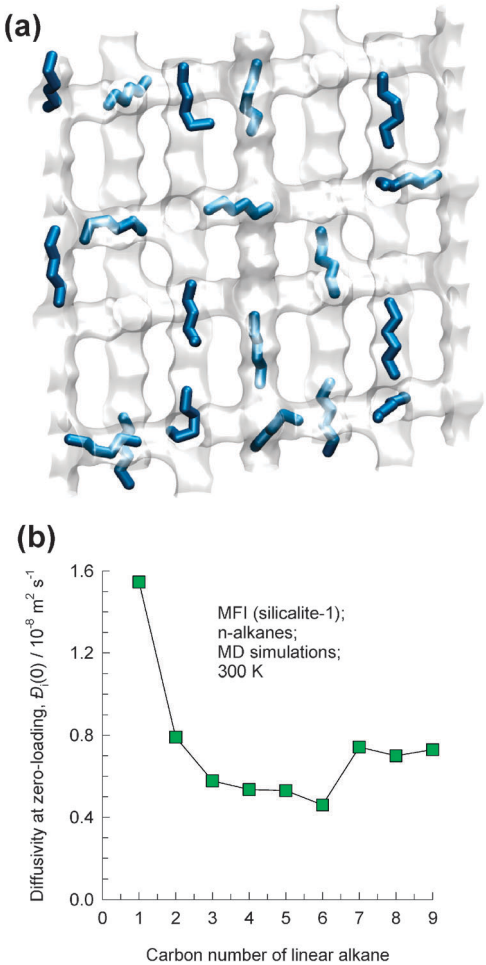

Fig. 14 (a) Snapshot showing the location of nC6 in MFI at a loading of 4 molecules per unit cell. (b) MD data for zero-loading diffusivities $Đ_i(0)$ of linear alkanes in MFI zeolite.[4]

Generally speaking, the surfaces offer additional resistances. The determination of transport across the surface layer requires the monitoring of transient concentration profiles during uptake or release (*via* interference microscopy) and tracer exchange (*via* IR microimaging). This approach has been used to investigate the surface resistance of Zn(tbip) and FER crystals.[37] Further research is required to examine how the surface diffusion characteristics relate to that within the bulk crystals.

5. Diffusion in binary mixtures

Maxwell–Stefan formulation and diffusivities

In porous materials, the diffusion characteristics of any component are influenced by its partner species. The key to the successful development of separation technologies is the proper description of such mutual influences. The most convenient expression for the fluxes N_i has roots in the pioneering works of James Clerk Maxwell and Josef Stefan for describing diffusion in *gaseous* mixtures:

$$-\phi \frac{c_i}{RT} \nabla \mu_i = \sum_{\substack{j=1 \\ j \neq i}}^{2} \frac{x_j N_i - x_i N_j}{Đ_{12}} + \frac{N_i}{Đ_i}; \quad i = 1, 2 \qquad (14)$$

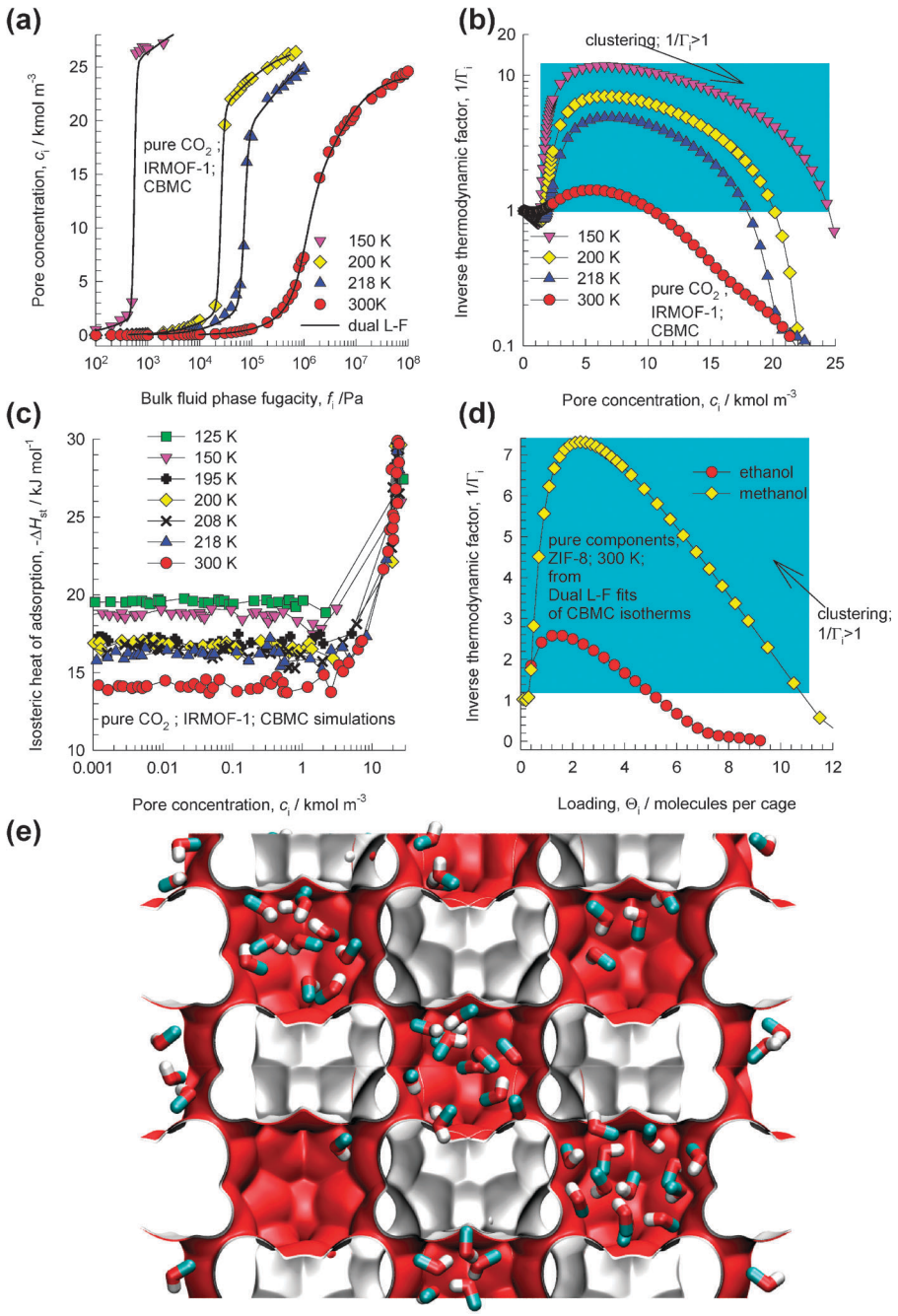

Fig. 15 (a) CBMC simulations of pure component isotherms for CO_2 adsorption in IRMOF-1 at different temperatures, T. Also shown are the fits using eqn (13). (b) The inverse thermodynamic factor, $1/\Gamma_i$, for CO_2 adsorption in IRMOF-1 at different T, obtained from analytic differentiation of the dual-Langmuir–Freundlich fits. (c) CBMC simulations of the isosteric heats of adsorption of CO_2 IRMOF-1 at different T. (d) The inverse thermodynamic factor, $1/\Gamma_i$, for methanol and ethanol adsorption in ZIF-8, obtained from analytic differentiation of the dual-Langmuir–Freundlich fits. (e) Snapshot showing the equilibrium positions of adsorbed methanol molecules in ZIF-8.

where x_i are the component mole fractions in the *adsorbed* phase

$$x_i = c_i/c_t; \quad c_t = c_1 + c_2; \quad i = 1,2 \qquad (15)$$

The $Đ_i$ has the same physical meaning as for unary diffusion, and characterizes the interactions that species i experiences with the constraining pore wall. Most commonly, the $Đ_i$ in the mixture corresponds to the value of the pure component i, and consequently this can be estimated from *unary* diffusion experiments or simulations. In cases where molecular clustering occurs, or in the case of segregated adsorption, the $Đ_i$ in the mixture can be lower than that of pure components; this aspect will be discussed later. The $Đ_{12}$ quantify intermolecular interactions; these *mutual* exchange coefficients reflect how the facility for transport of species 1 *correlates* with that of species 2. All the diffusivities defined in eqn (14) can be obtained explicitly and the procedure is provided in the ESI.†

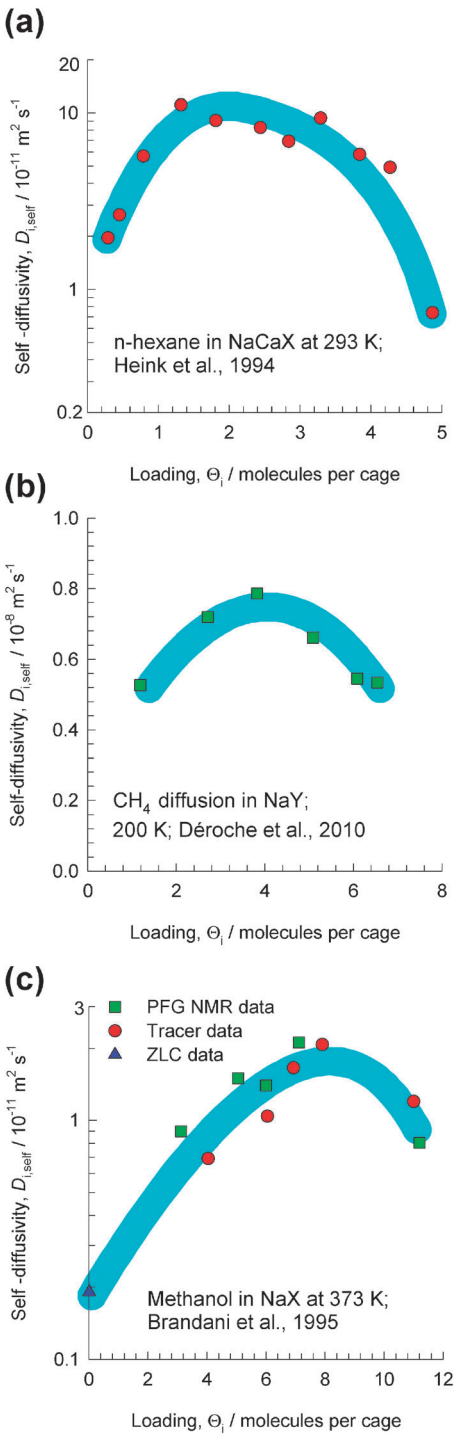

Fig. 16 Experimental data for the concentration dependence of self-diffusivities for various guest–host structures. (a) Diffusion of *n*-hexane (*n*C6) in NaCaX (75 Ca atoms).[53] (b) Diffusion of CH_4 in NaY at 200 K.[54] (c) Diffusion of methanol in NaX.[34]

In order to illustrate the importance of correlation effects, Fig. 18 presents MD simulation data for the M–S diffusivities, $Đ_1$, $Đ_2$, and $Đ_{12}$, for diffusion of CH_4/H_2 mixtures in four different materials: mesoporous BTP-COF, and microporous MgMOF-74, FAU-Si, and MFI. In the limit of low concentrations, say $c_t < 1$ kmol m^{-3}, we have $Đ_{12} \gg Đ_2 > Đ_1$ in all four materials. Consequently, the contribution of the first right

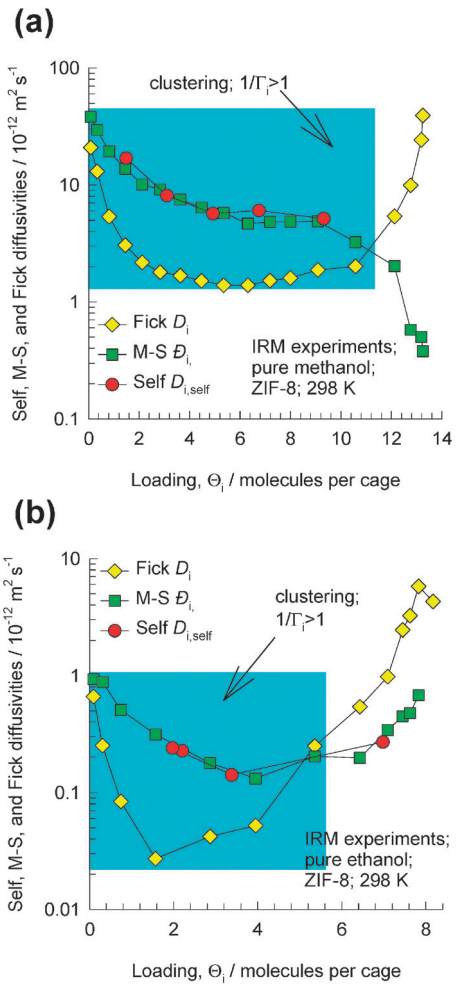

Fig. 17 Loading dependence of $Đ_i$, D_i, and $D_{i,self}$ for (a) methanol and (b) ethanol in ZIF-8.[55]

member of eqn (14) can be considered to be negligible, and consequently the flux of species 1 is not "coupled" to that of species 2, and we have

$$N_i = -\phi Đ_i \frac{c_i}{RT} \nabla \mu_i; \quad \text{correlations negligible} \qquad (16)$$

For mixture diffusion under conditions such that the pore concentrations of both components are negligibly small, we can safely ignore mutual diffusional influences and assume that each component diffuses independently of its partner species. For membrane separations, for example, we can take the unary permeance data to be representative of permeance of that species in the mixture.

For all four materials, the exchange coefficient $Đ_{12}$ shows a significant reduction in magnitude with increasing values of c_t. This implies that the first right member of eqn (14) makes increasing contributions to the fluxes. Put another way, coupling, or correlation, effects become increasingly important as c_t increases. But the influence of correlations is not the same for *both* species, as will be evident on closer examination of the data in Fig. 18. For all four materials, the M–S diffusivity of CH_4, $Đ_1$, is lower than the binary exchange coefficient $Đ_{12}$. Consequently, the influence of the first right member of eqn (14) on the flux of CH_4 is relatively small, *i.e.* coupling effects

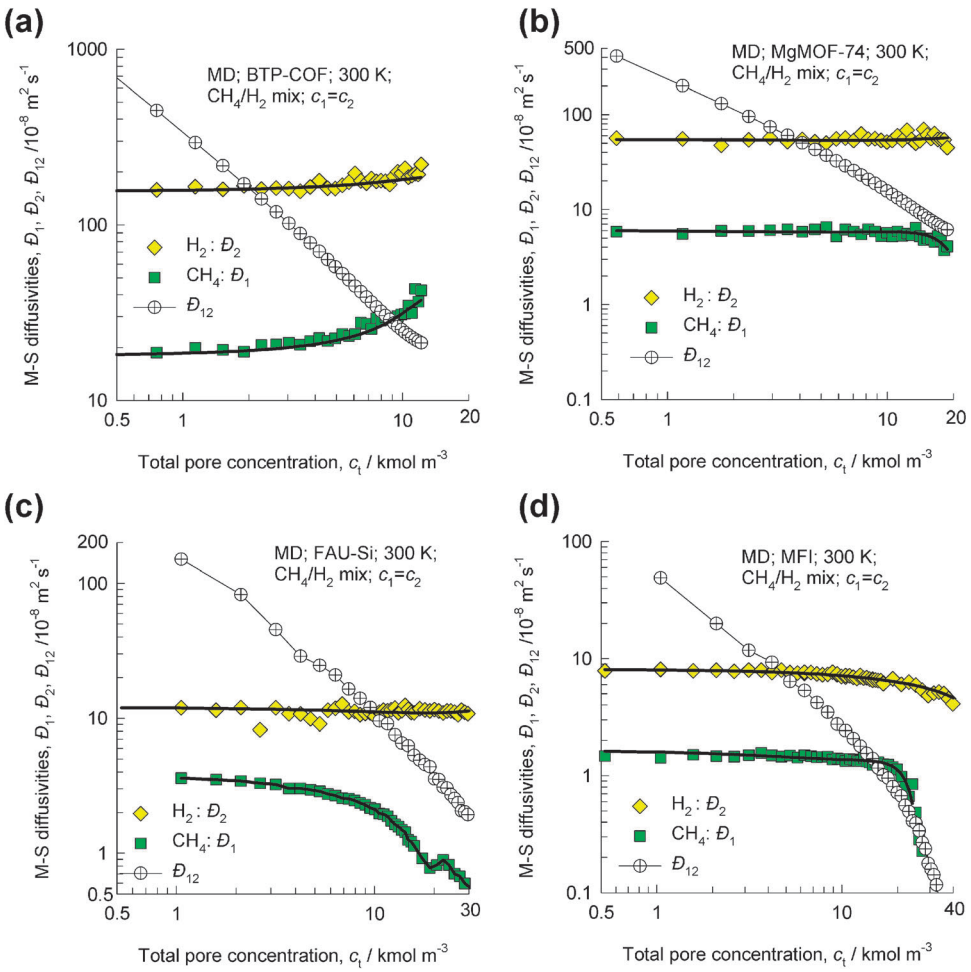

Fig. 18 MD data on M–S diffusivities, $Đ_1$, $Đ_2$, and $Đ_{12}$, for diffusion of CH_4/H_2 mixtures in (a) BTP-COF, (b) MgMOF-74, (c) FAU-Si, and (d) MFI as a function of the total concentration, c_t.[8]

are not expected to have a significant effect on CH_4 flux in the mixture diffusion. The situation with regard to H_2 is completely different. With increased c_t, the binary exchange coefficient $Đ_{12}$ is lowered to values below that of the M–S diffusivity of H_2, $Đ_2$. Consequently, the influence of the first right member of eqn (14) on the flux of H_2 is very significant at high values of c_t. In binary mixture diffusion the flux of H_2 is significantly influenced by the presence of the tardier CH_4. Generally speaking, coupling effects have a more telling influence on the more mobile partner species; this conclusion is of generic validity.[8]

Formally, eqn (14) applies to both meso- and micro-porous materials; there are however differences in detail. Fig. 19a compares the exchange coefficient $Đ_{12}$ for the CH_4/H_2 mixture in a few chosen micro- and meso-porous materials with the corresponding *fluid* phase diffusivity $Đ_{12,fl}$ at the same total pore concentration, c_t. In mesoporous BTP-COF, the values of the exchange coefficient $Đ_{12}$ are nearly the same as the binary *fluid phase* M–S diffusivity, $Đ_{12,fl}$, over the entire range of c_t. The approximation $Đ_{12} \approx Đ_{12,fl}$ holds for a wide variety of guest mixtures in mesopores.[7] Indeed, the widely used Dusty Gas Model for diffusion in mesoporous materials is obtained from eqn (14) by invoking the assumption $Đ_{12} = Đ_{12,fl}$, along with the Knudsen prescription, $Đ_i = D_{i,Kn}$. For micro-porous materials, the $Đ_{12}$ is lower than the corresponding fluid phase diffusivity $Đ_{12,fl}$ because the species i–species j correlations are also significantly influenced by species i–wall interactions. Within the 5.5 Å channels of MFI zeolite, the $Đ_{12}$ is about a tenth of the value for $Đ_{12,fl}$. The data in Fig. 19a are analogous to those for the self-exchange coefficients, $Đ_{ii}$, of the constituent species. Indeed, $Đ_{12}$ can be estimated by interpolating between the self-exchange coefficients of pure components:

$$Đ_{12} = (Đ_{11})^{x_1}(Đ_{22})^{x_2} \quad (17)$$

Eqn (17) has its origin in the logarithmic interpolation for the composition dependence of the M–S diffusivity for non-ideal binary mixtures as a function of the liquid phase mole fraction.[4] As illustration, Fig. 19b compares the Vignes interpolation estimations of $Đ_{12}$ for CH_4/H_2 mixture diffusion in MFI with MD simulated values; the agreement is representative of a wide range of guest–host combinations and good enough for practical use.[7]

Slowing-down and hindering effects

Applying eqn (14) to describe equimolar diffusion ($N_1 + N_2 = 0$) in a system consisting of two species, tagged and un-tagged, that are identical with respect to diffusional properties yields

$$-\frac{c_1}{RT}\nabla\mu_1 = \frac{(x_1 + x_2)N_1}{Đ_{11}} + \frac{N_1}{Đ_1} = \left(\frac{1}{Đ_{11}} + \frac{1}{Đ_1}\right)N_1 \quad (18)$$

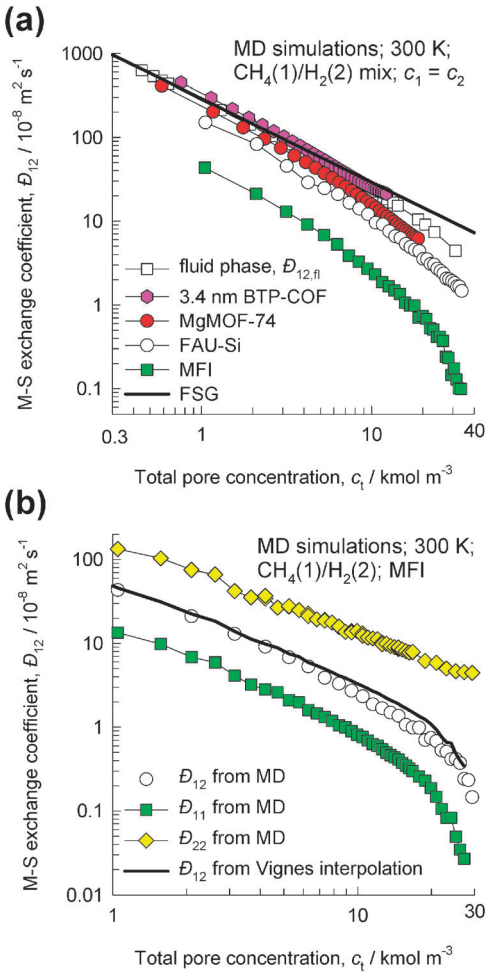

Fig. 19 (a) The M–S exchange coefficients $Đ_{12}$, for diffusion of CH_4/H_2 mixtures in a variety of host materials, as a function of the total pore concentration, c_t.[8] The $Đ_{12,fl}$ for binary *fluid phase* mixture diffusion, obtained from independent MD simulations, are also presented. The calculation of $Đ_{12,fl}$ using correlation of Fuller, Schettler and Giddings (FSG),[50] developed for *binary* gas mixtures, is indicated by the continuous solid line. (b) Comparison of the MD simulated $Đ_{12}$ for MFI with the estimations of the Vignes interpolation eqn (17).

Eqn (18) defines the self-diffusivity $D_{i,\text{self}}$ within a pore

$$-\frac{c_i}{RT}\nabla\mu_i = \frac{N_i}{D_{i,\text{self}}} \tag{19}$$

and we obtain eqn (3) for *unary* self-diffusivity. The corresponding result for a *binary* mixture of *i* and *j* accounts for the set of interactions: (a) species *i*–wall, (b) species *i*–species *i*, and (c) species *i*–species *j*:

$$\begin{aligned}\frac{1}{D_{1,\text{self}}} &= \frac{1}{Đ_1}+\frac{x_1}{Đ_{11}}+\frac{x_2}{Đ_{12}};\\ \frac{1}{D_{2,\text{self}}} &= \frac{1}{Đ_2}+\frac{x_2}{Đ_{22}}+\frac{x_1}{Đ_{12}}\end{aligned} \tag{20}$$

The self-diffusivities $D_{i,\text{self}}$ in the mixture are determinable from monitoring the mean square displacements, and the formula is the same as for unary diffusion, given by eqn (2). The $D_{i,\text{self}}$ of the more mobile species is lowered due to correlations with the tardier partner. Conversely, the $D_{i,\text{self}}$ of the tardier species is increased due to correlations with the more mobile partner. The net result is that the self-diffusivities of components in a mixture are closer together than the corresponding unary values. This is illustrated in Fig. 20a for CO_2/H_2 equimolar mixture diffusion in MFI. With increasing c_t, the $D_{i,\text{self}}$ values for the binary mixture approach

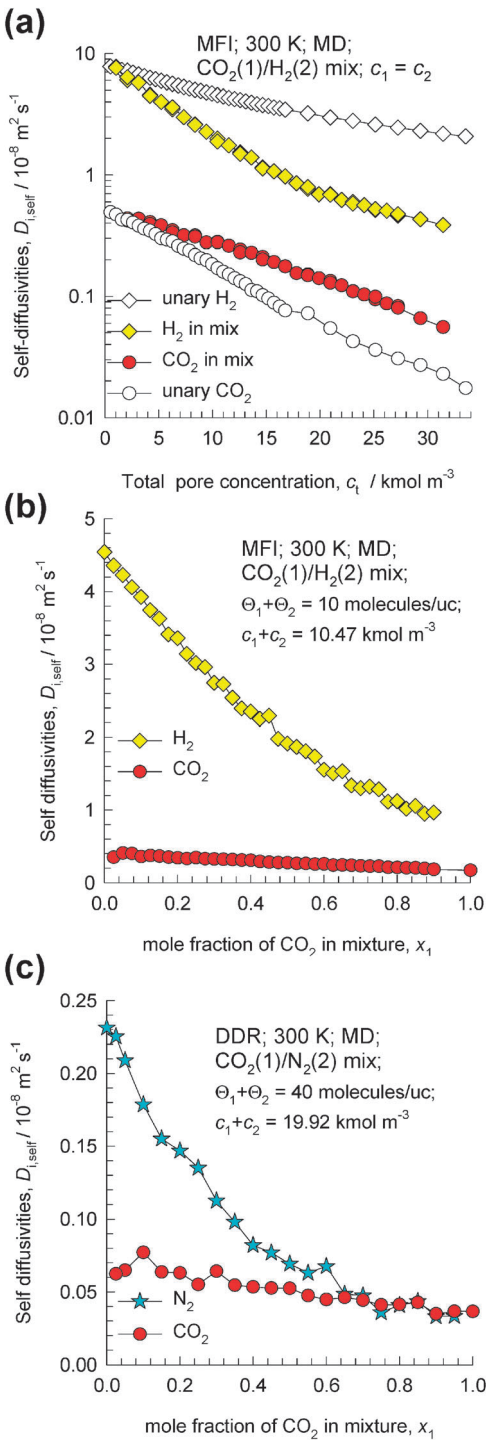

Fig. 20 MD data on self-diffusivities for (a) equimolar CO_2/H_2 mixtures in MFI, (b) CO_2/H_2 mixtures at constant c_t in MFI and (c) CO_2/N_2 mixtures at constant c_t in DDR.[8]

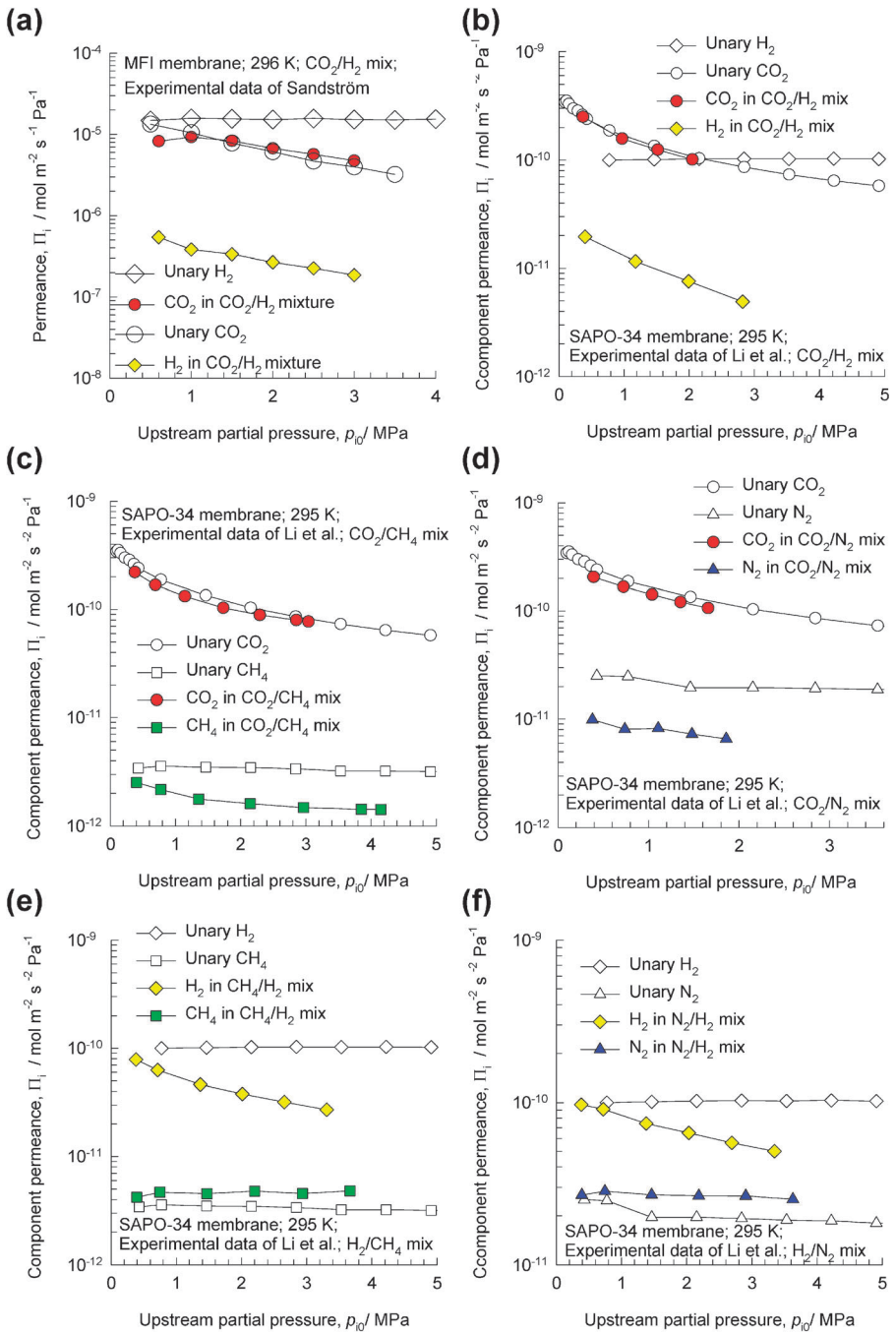

Fig. 21 Comparison of the permeances of pure components with those in (a, b) CO_2/H_2, (c) CO_2/CH_4, (d) CO_2/N_2, (e) CH_4/N_2, and (f) H_2/N_2 mixtures across (a) MFI and (b, c, d,e,f) SAPO-34 membranes. The MFI permeation data are from Sandström *et al.*[56] The SAPO-34 permeation data are from Li *et al.*[57]

each other and are much closer together than the corresponding unary values. CO_2 is the tardier species in the mixture, and with increasing proportion of CO_2 in the adsorbed phase the slowing-down effect on the more mobile partner H_2 increases; this is demonstrated in the data in Fig. 20b at constant c_t. With a preponderance of CO_2 within the pores of MFI, the diffusivity of H_2 is reduced by a factor of about 5, when compared to the value for pure H_2. The slowing-down effect caused by CO_2 in DDR zeolite is much more severe because of preferential perching of CO_2 at the window regions (*cf.* snapshot in Fig. 8c). This hindering effect of CO_2 on the mobility of partner molecules is illustrated in Fig. 20c for CO_2/N_2 mixtures. We note that when more than 50% of the adsorbed phase consists of CO_2, the self-diffusivities of both species are practically identical and dictated by the hopping of CO_2 across the windows. The preferential perching of CO_2 at the window regions, and consequent hindering of partner species, are best appreciated by viewing the video animations for CO_2/H_2, CO_2/CH_4, and CO_2/N_2 mixture diffusion in DDR, available as ESI.†

Slowing down and hindering effects are of significant importance for CO_2 capture using membranes. As illustration, Fig. 21a and b compare the permeances, defined by

$$\Pi_i \equiv N_i/(p_{i0} - p_{i\ell}), \qquad (21)$$

of pure components with those in CO_2/H_2 mixtures across MFI and SAPO-34 (iso-structural with CHA) membranes.[8] We note that the permeance of the tardier CO_2 in the mixture is practically the same as that for unary diffusion for the entire range of upstream partial pressures. For H_2, the permeance in the mixture is about an order of magnitude lower than for unary diffusion. Furthermore, we note that the H_2 permeance in the mixture is progressively reduced as the upstream pressure is increased. Increased upstream pressure implies higher concentration of components inside the pores of MFI and SAPO-34, with consequent increase in the correlation effects. Analogous conclusions hold for CO_2/CH_4, CO_2/N_2, CH_4/N_2, and H_2/N_2 mixture permeation; see Fig. 21c–f for SAPO-34 experimental data. For CO_2/CH_4 separation with DDR membranes, the experimental permeation data can only be explained if hindering effects caused by perching of CO_2 at the window regions are accounted for. The success of membrane technologies for CO_2 capture rests on the proper *quantitative* modeling of correlation effects.[8] For CO_2-selective separation of CO_2/N_2, CO_2/CH_4, and CO_2/H_2 mixtures it is advantageous to choose pore sizes and connectivities that result in high degrees of correlations because this will have the effect of slowing-down the more mobile partners N_2, CH_4, and H_2. For this purpose the information presented in Fig. 3 is of use. These data also explain the potential of MgMOF-74 due to strong correlations within 1D channels.[8]

Intersection blocking and traffic-junction effects

In the PFG NMR investigation of Fernandez *et al.*[38] the self-diffusivity in MFI of *n*-butane (nC4), in mixtures with iso-butane (iC4), was found to decrease to nearly zero as the loading of iC4 is increased from $\Theta_{iC4} = 0$ to 2 molecules per unit cell; see Fig. 22a. The reason for this strong decline can be understood on the basis of the preferential location of iC4 at the channel intersections of MFI. For $\Theta_{iC4} = 2$, half of the total number of intersections are occupied by iC4 that has a diffusivity which is about three orders of magnitude lower than that of nC4. Since the occupancy of the intersections is distributed randomly, each of the straight channels has an

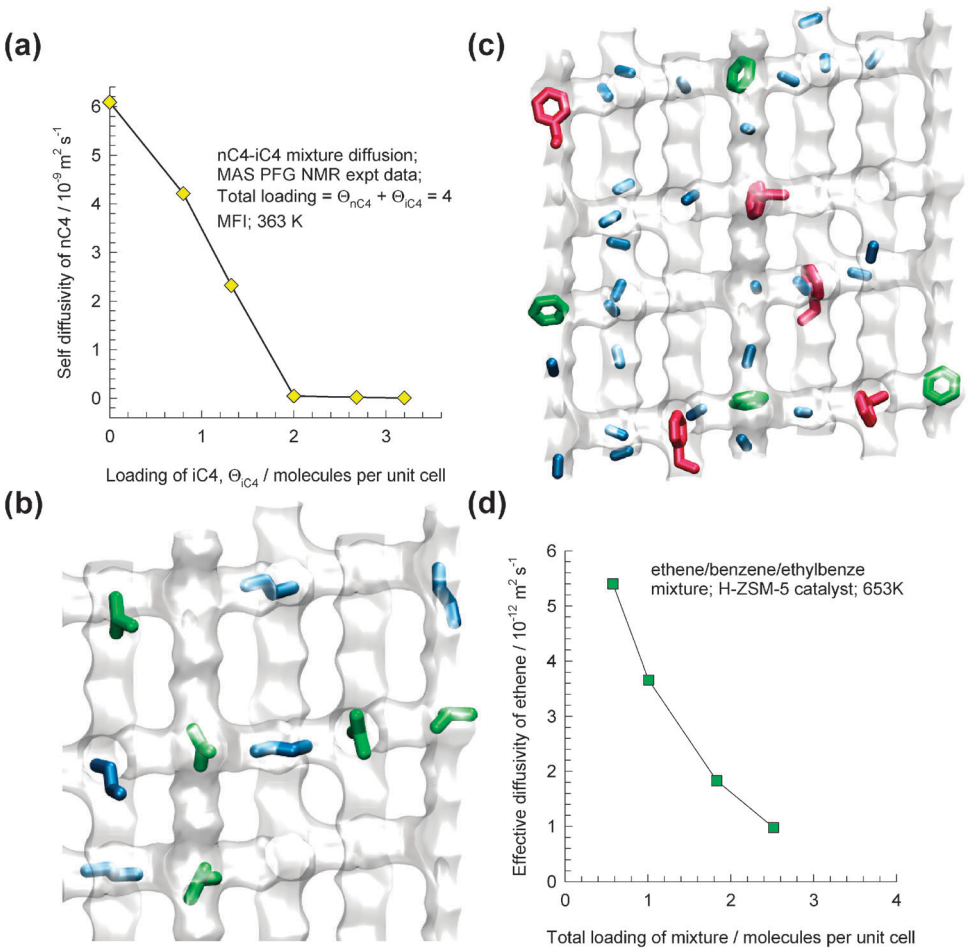

Fig. 22 (a) Experimental data[38] on self-diffusion coefficients of *n*C4 in *n*C4–iC4 mixtures in MFI as a function of the loading of iC4 in the mixture. (b) Snapshots showing the location of nC4 and iC4 molecules in MFI. (c) Snapshot showing the location of reactants and products in the alkylation of benzene with ethene to produce ethylbenzene within the intersecting channel topology of MFI catalyst. (d) Effective diffusivity of ethene within the MFI catalyst as a function of the mixture loading.[43]

iC4 molecule ensconced somewhere along the channels; this is evident from the snapshot in Fig. 22b, showing that all channels have at least one iC4 molecule along their length. This is tantamount to blockage and leads to severe reduction in the molecular traffic of the intrinsically more mobile nC4. Uptake experiments of Chmelik *et al.*[39] provide further evidence of the influence iC4 has on co-diffusion of nC4 in MFI crystals. PFG NMR studies of Förste *et al.*[40] found that the self-diffusivity of CH_4 in MFI is significantly reduced as the loading of the co-adsorbed benzene increases; the explanation is again to be found in the hindering of CH_4 diffusion due to blocking of the intersections by benzene.[40] Video animations of CH_4/benzene mixture diffusion in MFI, available as ESI†, demonstrates the blocking effect due to benzene molecules at the intersections. For analogous reasons, the branched alkanes 2-methylpentane (2MP) and 3-methylpentane (3MP) cause the reduction in the self-diffusivity of the n-hexane (nC6) in nC6–2MP, and nC6–3MP mixtures.[41] Intersection blocking by branched and cyclic hydrocarbons is a plausible explanation for the observed inhibition of the cracking of *n*-octane using an MFI catalyst.[42]

Traffic junction effects are of vital importance in modeling reactors for alkylation of benzene with ethene using the MFI zeolite catalyst (in the acidic form H-ZSM-5) to produce ethylbenzene.[43] Both benzene (reactant) and ethylbenzene (product) are preferentially located at the intersections of MFI; see Fig. 22c. The blocking of intersections causes effective diffusivity of ethene inside the catalyst to reduce five-fold as the total mixture loading approaches 2 molecules per unit cell; see Fig. 22d.

Mutual slowing-down effects

For water–alcohol mixture diffusion, the diffusivity of each component is lowered due to hydrogen bonding. This is illustrated in Fig. 23 for water–methanol diffusion in DDR and CHA; we note significant reductions in each of the diffusivities with increasing amounts of partner species. The practical consequences are that in membrane pervaporation, the fluxes of *both* components in the feed mixture are lowered due to the presence of partner species. As illustration, Fig. 23c presents data on permeation fluxes for water–methanol pervaporation across a CHA membrane.[44] Both water and methanol fluxes are reduced with increasing concentrations of partner species. Khajavi *et al.*[45] report experimental data on water–alcohol permeation across an H-SOD membrane. Their experiments show significant reduction in the water flux with increasing alcohol concentrations in the feed mixture (see Fig. 23d); this severe reduction is largely ascribable to molecular clustering. Similar experimental data for water–alcohol pervaporation across DDR[46] membranes are reported. The CHA, H-SOD,

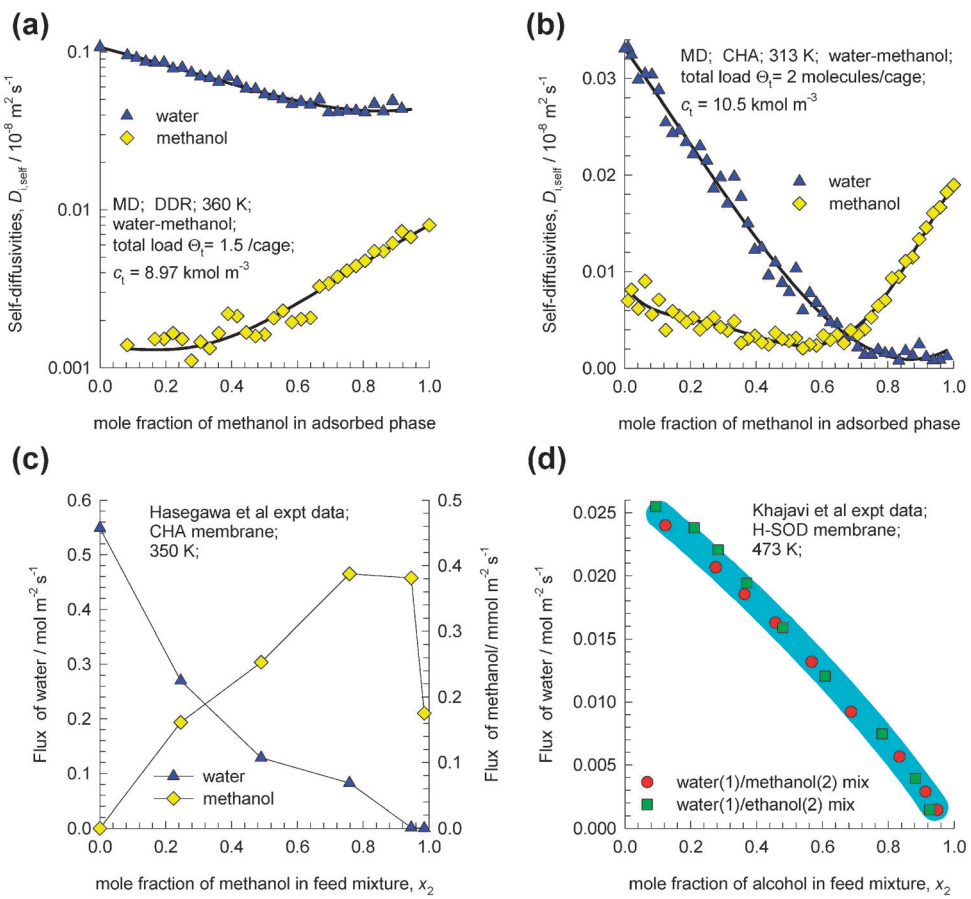

Fig. 23 Self-diffusivities, $D_{i,self}$, in water–methanol mixtures of varying composition in (a) DDR, and (b) CHA.[58] (c) Experimental data of Hasegawa *et al.*[44] for permeation fluxes across the CHA membrane as a function of the methanol mole fraction in water(1)/methanol(2) mixtures. (d) Experimental data of Khajavi *et al.*[45] for water flux across an H-SOD membrane as a function of the alcohol mole fraction in water(1)/methanol(2), and water(1)/ethanol(2) mixtures.

and DDR membrane pervaporation data are only explainable by allowing for *mutual* slowing-down effects caused by hydrogen bonding.

For transport across a Nafion membrane in methanol fuel cell applications, strong hydrogen bonding between water and methanol is evidenced by molecular simulations,[47] and NMR data on self-diffusivities in water provide further experimental confirmation of mutual slowing-down effects.[48] The mutual slowing down effects cannot be modeled by considering the exchange coefficients $Đ_{ij}$ alone; we need to account for lowering of the component $Đ_i$ due to the presence of partner species. Put another way, the $Đ_i$ in eqn (14) *cannot* be identified with the pure component values.

Yu *et al.*[49] found that their experimental data on permeation of methanol–acetone mixtures across an MFI membrane can only be rationalized if both the component $Đ_i$ are lowered in the mixture, when compared with the pure component values. The underlying cause of their findings is most likely to be due to the clustering caused by hydrogen bonding of acetone and methanol molecules.

6. Conclusions

Unary and mixture diffusion characteristics in a wide variety of crystalline meso- and micro-porous materials have been analysed using published MD and experimental data. The following major conclusions emerge.

(1) The Maxwell–Stefan diffusion (eqn (14)) provides a convenient unified description of mixture diffusion in both micro- and meso-porous materials. The approach uses pore concentrations c_i, expressed in terms of accessible pore volume inside the porous structures.

(2) The $Đ_i$ in eqn (14) reflects molecule–wall interactions. Except in cases where we have extreme segregated adsorption, or when strong molecular clustering occurs, the $Đ_i$ in eqn (14) can be identified with the *pure component* value at the same total concentration as in the mixture, c_t.

(3) For mesoporous materials, in the limit of low pore concentrations, the $Đ_i(0)$ corresponds to the classic Knudsen diffusivity, $D_{i,Kn}$, only when the molecule does not adsorb at the pore wall. With increasing adsorption strength, $Đ_i(0)$ can be appreciably lower than $D_{i,Kn}$.

(4) For micro-porous structures, the magnitude of $Đ_i$ is influenced by a variety of factors such as (a) degree of confinement, (b) binding energy, (c) presence of cations, and (d) commensurate–incommensurate considerations. The $Đ_i - c_i$ dependence is affected by adsorption equilibrium, isotherm inflection, and alteration in the free energy barriers for hopping of molecules.

(5) The exchange coefficients $Đ_{12}$ reflect molecule–molecule interactions, and consequently *correlation* effects. For mesopores $Đ_{12}$ equals the corresponding *fluid* phase diffusivity $Đ_{12,fl}$, determined at the same mixture loading c_t. For micropores, the $Đ_{12}$ is significantly lower than $Đ_{12,fl}$; the extent of lowering depends on the degree of confinement.

(6) For binary mixtures, correlation effects cause slowing-down of the more mobile species due to the presence of tardier molecules. Such slowing-down effects are of vital importance in membrane separation processes for CO_2 capture.

(7) Preferential location of branched hydrocarbons, benzenes, and cycloalkanes at the channel intersections causes partial, or total, blocking leading to sharp decline in the diffusivities of partner species. These traffic junction effects have important consequences in separations and catalysis.

(8) In water–alcohol mixture diffusion there is *mutual* slowing-down caused by hydrogen bonding; these effects are of vital importance in membrane pervaporation processes.

Nomenclature

b_i	dual-Langmuir–Freundlich adsorption constant for species i, Pa^{-v_i}
c_i	concentration of species i, mol m^{-3}
$c_{i,sat}$	saturation capacity of species i, mol m^{-3}
c_t	total concentration in mixture, mol m^{-3}
d_p	pore diameter, m
D_i	Fick diffusivity of species i, m^2 s^{-1}
$D_{i,self}$	self-diffusivity of species i, m^2 s^{-1}
$Đ_{ii}$	self-exchange coefficient, m^2 s^{-1}
$Đ_{ii,fl}$	self-diffusivity of species i in the fluid phase, m^2 s^{-1}
$Đ_i$	M–S diffusivity, m^2 s^{-1}
$Đ_i(0)$	zero-loading M–S diffusivity, m^2 s^{-1}
$Đ_{12}$	M–S exchange coefficient defined by eqn (14), m^2 s^{-1}
$Đ_{12,fl}$	M–S diffusivity in a binary fluid mixture, m^2 s^{-1}
$D_{i,Kn}$	Knudsen diffusivity of species i, m^2 s^{-1}
f_i	fluid phase fugacity of species i, Pa
$-\Delta H_{st}$	isosteric heat of adsorption, J mol^{-1}
k_B	Boltzmann constant, 1.38×10^{-23} J $molecule^{-1}$ K^{-1}
n_i	number of molecules of species i in the simulation box, dimensionless
M_i	molar mass of species i, kg mol^{-1}
N_i	molar flux of species i, mol m^{-2} s^{-1}
p_i	partial pressure of species i, Pa
$\mathbf{r}_{l,i}(t)$	position vector for molecule l of species i at any time t, m
R	gas constant, 8.314 J mol^{-1} K^{-1}
t	time, s
T	absolute temperature, K
T_c	critical temperature, K
V_p	accessible pore volume, m^3 kg^{-1}
x_i	mole fraction of species i based on loading within pores, dimensionless

Greek letters

δE_i	reduction in energy barrier for diffusion, J mol^{-1}
ε	Lennard-Jones interaction energy parameter, J $molecule^{-1}$
Γ_i	thermodynamic factor, dimensionless
μ_i	molar chemical potential, J mol^{-1}
Π_i	permeance of species i, mol m^{-2} s^{-1} Pa^{-1}
θ_i	fractional occupancy of species i, dimensionless
Θ_i	loading of i, molecules per unit cell
σ	Lennard-Jones size parameter, m

Subscripts

0	referring to the upstream face of the membrane
fl	referring to the fluid phase

i	referring to component *i*
ℓ	referring to the downstream face of the membrane
t	referring to the total mixture
Kn	referring to Knudsen
sat	referring to saturation conditions

Acknowledgements

This material is based upon work supported as part of the Center for Gas Separations Relevant to Clean Energy Technologies, an Energy Frontier Research Center funded by the U.S. Department of Energy, Office of Science, Office of Basic Energy Sciences under Award Number DE-SC0001015.

References

1 J. Kärger, D. M. Ruthven and D. N. Theodorou, *Diffusion in Zeolites and Other Nanoporous Materials*, Wiley-VCH, Weinheim, 2012.
2 R. Krishna and J. M. van Baten, *Phys. Chem. Chem. Phys.*, 2011, **13**, 10593–10616.
3 D. Frenkel and B. Smit, *Understanding molecular simulations: from algorithms to applications*, 2nd edn, Academic Press, San Diego, 2002.
4 R. Krishna, *J. Phys. Chem. C*, 2009, **113**, 19756–19781.
5 O. Talu and A. L. Myers, *AIChE J.*, 2001, **47**, 1160–1168.
6 S. K. Bhatia and D. Nicholson, *Chem. Eng. Sci.*, 2011, **66**, 284–293.
7 R. Krishna and J. M. van Baten, *Chem. Eng. Sci.*, 2009, **64**, 3159–3178.
8 R. Krishna and J. M. van Baten, *J. Membr. Sci.*, 2011, **383**, 289–300.
9 H. Bux, C. Chmelik, R. Krishna and J. Caro, *J. Membr. Sci.*, 2011, **369**, 284–289.
10 H. Bux, C. Chmelik, J. M. Van Baten, R. Krishna and J. Caro, *Adv. Mater.*, 2010, **22**, 4741–4743.
11 N. Hedin, G. J. DeMartin, W. J. Roth, K. G. Strohmaier and S. C. Reyes, *Microporous Mesoporous Mater.*, 2008, **109**, 327–334.
12 C. Gücüyener, J. van den Bergh, J. Gascon and F. Kapteijn, *J. Am. Chem. Soc.*, 2010, **132**, 17704–17706.
13 J. J. Pluth and J. V. Smith, *J. Am. Chem. Soc.*, 1980, **102**, 4704–4708.
14 E. Beerdsen, D. Dubbeldam and B. Smit, *Phys. Rev. Lett.*, 2006, **96**, 044501.
15 A. Gupta, L. A. Clark and R. Q. Snurr, *Langmuir*, 2000, **16**, 3910–3919.
16 C. Chmelik, L. Heinke, J. Kärger, D. B. Shah, W. Schmidt, J. M. van Baten and R. Krishna, *Chem. Phys. Lett.*, 2008, **459**, 141–145.
17 D. B. Shah, C. J. Guo and D. T. Hayhurst, *J. Chem. Soc., Faraday Trans.*, 1995, **91**, 1143–1146.
18 R. C. Runnebaum and E. J. Maginn, *J. Phys. Chem. B*, 1997, **101**, 6394–6408.
19 H. Jobic and D. N. Theodorou, *Microporous Mesoporous Mater.*, 2006, **102**, 21–50.
20 K. Yoo, R. Tsekov and P. G. Smirniotis, *J. Phys. Chem. B*, 2003, **107**, 13593–13596.
21 R. L. Gorring, *J. Catal.*, 1973, **31**, 13–26.
22 D. Dubbeldam and B. Smit, *J. Phys. Chem. B*, 2003, **107**, 12138–12152.
23 H. Jobic, A. Methivier, G. Ehlers, B. Farago and W. Haeussler, *Angew. Chem., Int. Ed.*, 2004, **43**, 364–366.
24 O. Talu, M. S. Sun and D. B. Shah, *AIChE J.*, 1998, **44**, 681–694.
25 H. Jobic, C. Laloué, C. Laroche, J. M. van Baten and R. Krishna, *J. Phys. Chem. B*, 2006, **110**, 2195–2201.
26 K. S. Walton, A. R. Millward, D. Dubbeldam, H. Frost, J. J. Low, O. M. Yaghi and R. Q. Snurr, *J. Am. Chem. Soc.*, 2008, **130**, 406–407.
27 T. A. Steriotis, K. L. Stefanopoulos, N. K. Kanellopoulos and A. C. Mitropoulos, *Colloids Surf., A*, 2004, **241**, 239–244.
28 J. Getzschmann, I. Senkovska, D. Wallacher, M. Tovar, D. Fairen-Jimenez, T. Düren, J. M. van Baten, R. Krishna and S. Kaskel, *Microporous Mesoporous Mater.*, 2010, **136**, 50–58.
29 R. Krishna and J. M. van Baten, *Langmuir*, 2010, **26**, 10854–10867.
30 M. Fleys, R. W. Thompson and J. C. MacDonald, *J. Phys. Chem. B*, 2004, **108**, 12197–12203.
31 R. Krishna and J. M. van Baten, *Langmuir*, 2010, **26**, 3981–3992.
32 J. Kärger and H. Pfeifer, *Zeolites*, 1987, **7**, 90–107.
33 R. Krishna and J. M. van Baten, *Microporous Mesoporous Mater.*, 2011, **142**, 745–748.
34 S. Brandani, D. M. Ruthven and J. Kärger, *Zeolites*, 1995, **15**, 494–495.
35 F. Salles, H. Jobic, A. Ghoufi, P. L. Llewellyn, C. Serre, S. Bourrelly, G. Férey and G. Maurin, *Angew. Chem., Int. Ed.*, 2009, **48**, 8335–8339.
36 F. Salles, H. Jobic, T. Devic, P. L. Llewellyn, C. Serre, G. Férey and G. Maurin, *ACS Nano*, 2010, **4**, 143–152.
37 L. Heinke, D. Tzoulaki, C. Chmelik, F. Hibbe, J. M. van Baten, H. Lim, J. Li, R. Krishna and J. Kärger, *Phys. Rev. Lett.*, 2009, **102**, 065901.
38 M. Fernandez, J. Kärger, D. Freude, A. Pampel, J. M. van Baten and R. Krishna, *Microporous Mesoporous Mater.*, 2007, **105**, 124–131.
39 C. Chmelik, L. Heinke, J. M. van Baten and R. Krishna, *Microporous Mesoporous Mater.*, 2009, **125**, 11–16.
40 C. Förste, A. Germanus, J. Kärger, H. Pfeifer, J. Caro, W. Pilz and A. Zikánová, *J. Chem. Soc., Faraday Trans.*, 1987, **83**, 2301–2309.
41 A. O. Koriabkina, A. M. de Jong, D. Schuring, J. van Grondelle and R. A. van Santen, *J. Phys. Chem. B*, 2002, **106**, 9559–9566.
42 S. Namba, K. Sato, K. Fujita, J. H. Kim and T. Yashima, *Stud. Surf. Sci. Catal.*, 1986, **28**, 661–668.
43 N. Hansen, R. Krishna, J. M. van Baten, A. T. Bell and F. J. Keil, *J. Phys. Chem. C*, 2009, **113**, 235–246.
44 Y. Hasegawa, C. Abe, M. Nishioka, K. Sato, T. Nagase and T. Hanaoka, *J. Membr. Sci.*, 2010, **364**, 318–324.
45 S. Khajavi, J. C. Jansen and F. Kapteijn, *J. Membr. Sci.*, 2009, **326**, 153–160.
46 J. Kuhn, J. M. Castillo-Sanchez, J. Gascon, S. Calero, D. Dubbeldam, T. J. H. Vlugt, F. Kapteijn and J. Gross, *J. Phys. Chem. C*, 2009, **113**, 14290–14301.
47 P. Y. Chen, C. P. Chiu and C. W. Hong, *J. Electrochem. Soc.*, 2008, **155**, B1255–B1263.
48 F. Hallberg, T. Vernersson, E. T. Pettersson, S. V. Dvinskikh, G. Lindbergh and I. Furó, *Electrochim. Acta*, 2010, **55**, 3542–3549.
49 M. Yu, J. L. Falconer, R. D. Noble and R. Krishna, *J. Membr. Sci.*, 2007, **293**, 167–173.
50 E. N. Fuller, P. D. Schettler and J. C. Giddings, *Ind. Eng. Chem.*, 1966, **58**, 19–27.
51 R. Krishna and J. M. van Baten, *J. Membr. Sci.*, 2011, **377**, 249–260.
52 H. Yucel and D. M. Ruthven, *J. Colloid Interface Sci.*, 1980, **74**, 186–195.
53 W. Heink, J. Kärger, S. Ernst and J. Weitkamp, *Zeolites*, 1994, **14**, 320–325.
54 I. Déroche, G. Maurin, B. J. Borah, H. Jobic and S. Yashonath, *J. Phys. Chem. C*, 2010, **114**, 5027–5034.
55 C. Chmelik, H. Bux, J. Caro, L. Heinke, F. Hibbe, T. Titze and J. Kärger, *Phys. Rev. Lett.*, 2010, **104**, 085902.
56 L. Sandström, E. Sjöberg and J. Hedlund, *J. Membr. Sci.*, 2011, **380**, 232–240.
57 S. Li, J. L. Falconer, R. D. Noble and R. Krishna, *J. Phys. Chem. C*, 2007, **111**, 5075–5082.
58 R. Krishna and J. M. van Baten, *J. Phys. Chem. C*, 2010, **114**, 13154–13156.

